The Millimeter/X-Ray Relation in Rapidly Accreting Supermassive Black Holes at z < 0.16

Citation for the original published paper (version of record):
Venselaar, S., Ricci, C., Del Palacio, S. et al (2026). The Millimeter/X-Ray Relation in Rapidly Accreting Supermassive Black Holes at z < 0.16. Astrophysical Journal, 1005(1).
http://dx.doi.org/10.3847/1538-4357/ae6da8

The Astrophysical Journal, 1005:48 (21pp), 2026 July 1 https://doi.org/10.3847/1538-4357/ae6da8

The Millimeter/X-Ray Relation in Rapidly Accreting Supermassive Black Holes at $z < 0.16$

Sophie M. Venselaar[1,2], Claudio Ricci[1,2,3], Santiago Del Palacio[4], Kriti K. Gupta[5,6,7], Chin-Shin Chang[8,9], Roberto Serafinelli[1,10], Macon A. Magno[11,12], Richard Mushotzky[13], Elena Shablovinskaya[14], Taiki Kawamuro[15], Ezequiel Treister[16], Jacob S. Elford[1], Susanne Aalto[17], George C. Privon[18,19,20], and Michael J. Koss[21]

[1] Instituto de Estudios Astrofísicos, Facultad de Ingeniería y Ciencias, Universidad Diego Portales, Av. Ejército Libertador 441, Santiago, Chile; sophie.venselaar@unige.ch
[2] Department of Astronomy, University of Geneva, ch. d'Ecogia 16, 1290 Versoix, Switzerland
[3] Kavli Institute for Astronomy and Astrophysics, Peking University, Beijing 100871, People's Republic of China
[4] Department of Space, Earth and Environment, Chalmers University of Technology, 412 96 Gothenburg, Sweden
[5] STAR Institute, Liège Université, Quartier Agora - Allée du six Août, 19c, B-4000 Liège, Belgium
[6] Sterrenkundig Observatorium, Universiteit Gent, Krijgslaan 281 S9, B-9000 Gent, Belgium
[7] Leibniz-Institut für Astrophysik Potsdam (AIP), An der Sternwarte 16, D-14482 Potsdam, Germany
[8] Department of Astronomy, University of Geneva, Chemin Pegasi 51, 1290 Versoix, Switzerland
[9] Joint ALMA Observatory, Avenida Alonso de Cordova 3107, Vitacura 7630355, Santiago, Chile
[10] INAF—Osservatorio Astronomico di Roma, Via Frascati 33, 00078, Monte Porzio Catone, Roma, Italy
[11] George P. and Cynthia Woods Mitchell Institute for Fundamental Physics and Astronomy, Texas A&M University, College Station, TX, 77845, USA
[12] CSIRO Space and Astronomy, ATNF, PO Box 1130, Bentley WA 6102, Australia
[13] Department of Astronomy, University of Maryland, College Park, MD 20742, USA
[14] Max-Planck-Institut für Radioastronomie, Auf dem Hügel 69, Bonn D-53121, Germany
[15] Department of Earth and Space Science, Osaka University, 1-1 Machikaneyama, Toyonaka 560-0043, Osaka, Japan
[16] Instituto de Alta Investigación, Universidad de Tarapacá, Casilla 7D, Arica, Chile
[17] Department of Space, Earth and Environment, Chalmers University of Technology, Onsala Space Observatory, 439 92, Onsala, Sweden
[18] National Radio Astronomy Observatory, 520 Edgemont Road, Charlottesville, VA 22903, USA
[19] Department of Astronomy, University of Virginia, 530 McCormick Road, Charlottesville, VA 22904, USA
[20] Department of Astronomy, University of Florida, P.O. Box 112055, Gainesville, FL 32611, USA
[21] Eureka Scientific, 2452 Delmer Street, Suite 100, Oakland, CA 94602-3017, USA

Received 2026 January 23; revised 2026 May 11; accepted 2026 May 11; published 2026 June 23

Abstract

A tight correlation between nuclear millimeter and X-ray emission has recently been found in nearby ($z < 0.01$) and low-Eddington ratio ($\lambda_{\rm Edd} < 0.1$) radio-quiet active galactic nuclei (AGNs), suggesting a common origin in the hot X-ray corona. We test this relation in nine more distant AGNs ($z \sim 0.06$–0.16) with higher bolometric luminosities ($\log(L_{\rm bol}/{\rm erg\ s^{-1}}) = 45.3$–$46.3$), Eddington ratios ($\lambda_{\rm Edd} = 0.19$–$0.85$), and X-ray bolometric corrections ($\kappa = 29$–194), selected from the Burst Alert Telescope (BAT) survey. We obtained observations with Swift at 2–10 keV and quasi-simultaneous observations with the Atacama Large Millimeter/submillimeter Array at 100 GHz with high angular resolution ($<0''.14$ arcsec). We find that these high-luminosity AGNs lie above the millimeter/X-ray correlation defined by lower-luminosity sources. A joint fit to both samples yields a second-degree polynomial with an intrinsic scatter of 0.32 dex. Furthermore, the millimeter emission correlates linearly with both the UV disk luminosity and $L_{\rm bol}$, with intrinsic scatters of 0.45 and 0.35 dex, respectively. We propose that the deviation from the linear millimeter/X-ray relation arises from a two-component coronal electron population: thermal electrons that produce X-rays, but become less efficient at higher luminosities, and nonthermal electrons that produce millimeter emission and remain tied to $L_{\rm bol}$. Additional millimeter emission from outflow-driven shocks may also contribute, though spectral energy distribution modeling and spectral index studies favor a coronal origin.

Unified Astronomy Thesaurus concepts: Active galactic nuclei (16); X-ray active galactic nuclei (2035); Supermassive black holes (1663); Submillimeter astronomy (1647)

1. Introduction

Active galactic nuclei (AGNs) are found at the center of ~10% of local galaxies, and are some of the most luminous persistent sources of radiation in the Universe. They are powered by accretion onto supermassive black holes (SMBHs) and emit radiation over the full electromagnetic spectrum (e.g., review by R. C. Hickox & D. M. Alexander 2018). The key nuclear components of an AGN include the accretion disk surrounding the SMBH, which emits primarily in the optical and ultraviolet (UV) bands; the hot corona close to the SMBH, responsible for most of the X-ray emission; and the surrounding dusty torus, which radiates in the infrared (IR; e.g., review by C. Ramos Almeida & C. Ricci 2017; C. Ricci 2026).

AGNs can be categorized as jetted/radio-loud (RL) or nonjetted/radio-quiet (RQ) based on the presence or absence of a strong, relativistic radio jet and/or extended radio emission, which leads to observational differences in the radio, X-ray, and γ-ray bands (P. Padovani 2017). RQ AGNs do not show strong jets or radio lobes, making them typically $\sim 10^3$ times fainter in the radio regime when normalized by optical emission (F. Panessa et al. 2019). Additionally, RQ AGNs do not emit as bright in γ-rays (M. Ackermann et al. 2012; P. Padovani 2017; J.-R. Liu et al. 2025) and have a thermal cutoff in the X-ray band at energies ~50–200 keV (A. Malizia et al. 2014; C. Ricci et al. 2018). These RQ AGNs make up the majority of the AGN population, accounting for approximately ~90% of all AGNs (e.g., P. Padovani et al. 2011). However, despite their faint radio emission, RQ AGNs still ubiquitously emit unresolved nuclear millimeter emission on scales smaller than ~10–20 pc (e.g., F. Panessa et al. 2019; T. Kawamuro et al. 2022; C. Ricci et al. 2023).

One proposed origin of this unresolved millimeter emission is the compact ($R \sim 5-10\,R_{\rm g}$, with $R_{\rm g}$ the gravitational radius[22]) and hot[23] X-ray corona, located close to the SMBH (e.g., A. Laor & E. Behar 2008). Recently, the size of the millimeter continuum emitting source has been measured for an RQ AGN at $z \sim 0.658$ through microlensing and was indeed found to be extremely compact with a size of $R < 100R_{\rm g}$ (M. Rybak et al. 2025). The corona is believed to be heated through magnetic reconnections (e.g., T. Di Matteo 1998), though this remains a matter of debate (e.g., Y. Inoue & A. Doi 2018; Y. Inoue et al. 2024; M. Nhat Ly et al. 2026). In the corona, optical/UV photons from the accretion disk are Comptonized by hot electrons, scattering to higher energies and producing X-ray emission (e.g., J. I. Katz 1976; F. Haardt & L. Maraschi 1991). In the presence of a strong magnetic field, the electrons in the corona are expected to produce synchrotron emission as well (e.g., G. B. Field & R. D. Rogers 1993; A. Laor & E. Behar 2008; Y. Inoue & A. Doi 2014; F. Panessa et al. 2019). Optically thin synchrotron emission produces a power-law spectrum, $S_\nu \propto \nu^{-\alpha}$, with a spectral index $\alpha \sim 0.5$–1 (e.g., E. Behar et al. 2015). However, for a compact emitter as the corona, the emission becomes self-absorbed (synchrotron self-absorption; SSA) at frequencies of $\nu_{\rm SSA} \sim 100$–300 GHz, producing a spectral turnover that transitions from optically thin to optically thick emission, following $S_\nu \propto \nu^{2.5}$ (e.g., A. Laor & E. Behar 2008; Y. Inoue & A. Doi 2014). The exact location of this turnover peak in the spectrum depends on the properties of the SSA region, such as its size and the magnetic field strength (e.g., S. del Palacio et al. 2025). Recent observations have detected this peak (e.g., Y. Inoue & A. Doi 2018; S. del Palacio et al. 2025), together with rapid millimeter variability (e.g., R. D. Baldi et al. 2015; E. Behar et al. 2020; P. O. Petrucci et al. 2023; T. Michiyama et al. 2024; E. Shablovinskaya et al. 2024), both supporting the idea that synchrotron emission indeed originates from a compact and dense region. However, this coronal origin of the millimeter emission in RQ AGN has not yet been conclusively confirmed. Alternative explanations include, for example, emission from a very compact and low-power jet (e.g., F. Panessa et al. 2019) or an outflow from the X-ray corona (A. M. Hankla et al. 2026).

If both the millimeter and X-ray emission originate from the corona, a strong correlation between them would be expected. Initially, E. Behar et al. (2015) found a relation of $L_{95\rm GHz} = 10^{-4}L_{2-10\rm keV}$ for eight RQ AGNs, although E. Behar et al. (2018) later reported significant scatter when expanding the sample. T. Kawamuro et al. (2022) analyzed high-resolution Atacama Large Millimeter/submillimeter Array (ALMA) observations of 98 low-redshift ($z < 0.05$) AGNs at 230 GHz, resolving scales up to ~200 pc. They found a tight correlation between the 230 GHz and 14–150 keV luminosities with a scatter of 0.36 dex. Recently, C. Ricci et al. (2023, hereafter R23) used high-resolution ALMA observations, probing physical scales of <23 pc, to report an even tighter correlation (scatter of ~0.2 dex) between 100 GHz and X-ray emission in a sample of 26 nearby AGNs ($z < 0.01$). These results provided compelling evidence for a common physical origin of the millimeter and X-ray emission.

The observed millimeter/X-ray correlation could serve as a powerful tool for studying highly obscured AGNs since millimeter emission remains unaffected by obscuration up to column densities of $N_{\rm H} \sim 10^{27}\,{\rm cm}^{-2}$ (e.g., R. H. Hildebrand 1983). This is about 3 dex better than what can be achieved by hard-X-ray (>10 keV) studies, which are unaffected by obscuration up to $N_{\rm H} \sim 10^{24}\,{\rm cm}^{-2}$ (e.g., C. Ricci et al. 2015). Therefore, this correlation would enable the study of highly obscured AGNs through millimeter emission and could also serve as a probe of AGN power, as it appears to be independent of $N_{\rm H}$, black hole mass ($M_{\rm BH}$), star formation rate (SFR) and Eddington ratio ($\lambda_{\rm Edd} = L_{\rm bol}/L_{\rm Edd}$), following R23. Furthermore, it could be used to infer $N_{\rm H}$, providing valuable insights into the AGN's obscuration properties (R23), and to identify dual AGNs at subkiloparsec nuclear separations (e.g., M. J. Koss et al. 2023; M. Droguett-Callejas et al. 2026).

In addition to the millimeter/X-ray relation, the relationship between optical/UV and X-ray emission, which together define the bolometric luminosity ($L_{\rm bol}$), has been extensively studied for decades to fully understand the energy output of AGNs (e.g., H. Tananbaum et al. 1979; Y. Avni & H. Tananbaum 1982, 1986; B. J. Wilkes et al. 1994). Various studies have found that the optical/UV emission from the disk and the X-ray emission from the corona are tightly correlated among themselves and with $L_{\rm bol}$ (e.g., R. V. Vasudevan & A. C. Fabian 2007; E. Lusso et al. 2010; K. K. Gupta et al. 2024). One way to characterize the relative contributions of the optical/UV and X-ray emission to the total bolometric output is through bolometric corrections, such as the X-ray bolometric correction $\kappa_{\rm X} = L_{\rm bol}/L_{\rm X}$. The value of $\kappa_{\rm X}$ was found to remain approximately constant at $\kappa_{\rm X} \sim 10$ for bolometric luminosities up to $\log(L_{\rm bol}/L_\odot) > 11$ (F. Duras et al. 2020). Beyond this range, $\kappa_{\rm X}$ increases with increasing $L_{\rm bol}$ (e.g., F. Duras et al. 2020; K. K. Gupta et al. 2024, 2025). This suggested that, as the accretion rate increases, driven by the increased production of optical and UV photons from the accretion flow, the relative contribution of the corona to the total luminosity decreases. This deviation suggests that the properties of the corona change at higher accretion rates, which could be due to the saturation of the Comptonizing electrons or to UV-driven disk winds that deplete the corona (e.g., S. Martocchia et al. 2017; L. Zappacosta et al. 2020).

The correlations between X-ray and millimeter emission, as well as between X-ray and UV emission, are well established for low-$\lambda_{\rm Edd}$ AGNs. In more luminous AGNs, $\kappa_{\rm X}$ is known to increase, altering the optical/UV to X-ray relation. However, to date, it remains unclear how the millimeter emission behaves in these more luminous sources. To determine whether the nuclear millimeter emission in luminous AGNs is more strongly correlated with X-ray coronal emission or optical/UV disk emission, we need high spatial resolution

---

[22] The gravitational radius is defined as $R_{\rm g} = GM_{\rm BH}/c^2$.

[23] The temperature of the corona is typically 50–100 keV (e.g., C. Ricci et al. 2017; A. Tortosa et al. 2018)

Table 1
Source Sample and Main Parameters

(1) Source	(2) SWIFT ID	(3) z	(4) $\lambda_{\rm Edd}$	(5) κ_{2-10}	(6) $\log(L_{\rm bol})$ (erg $\rm s^{-1}$)	(7) $\log(L_{14-150\,\rm keV})$ (erg $\rm s^{-1}$)	(8) log(SFR) ($M_\odot$ $\rm yr^{-1}$)	(9) $\log(M_{\rm BH})$ ($M_\odot$)	(10) $\log(N_{\rm H})$ ($\rm cm^{-2}$)
Q 0119−286	SWIFT J0122.0−2818	0.116	0.85	194	46.3	44.6	<1.7	8.2	<20.0
PG 0026+129	SWIFT J0029.2+1319	0.142	0.32	50	46.2	44.8	1.5	8.5	<20.0
PG 0052+251	SWIFT J0054.9+2524	0.155	0.28	33	46.1	44.8	1.8	8.5	<20.0
Mrk 813	SWIFT J1427.5+1949	0.110	0.19	40	46.0	44.6	<1.1	8.5	<20.9
RHS 61	SWIFT J2325.6+2157	0.120	0.25	54	46.0	44.8	<1.5	8.4	<21.1
LEDA 126226	SWIFT J1416.9−1158	0.098	0.26	29	45.7	44.6	<1.1	8.1	<20.0
2MASX J02223523+2508143	SWIFT J0222.3+2509	0.060	0.19	54	45.5	44.1	<0.7	8.1	<20.0
2MASX J17311341+1442561	SWIFT J1731.3+1442	0.080	0.42	60	45.4	44.2	<1.9	7.6	<20.0
LEDA 12773	SWIFT J0325.0−4154	0.058	0.30	70	45.3	43.7	0.7	7.7	20.0

Note. (1) Source name, (2) Swift ID, (3) Redshift, (4) Eddington ratio, (5) 2–10 keV bolometric correction, (6) Bolometric luminosity (all from G24), (7) BAT luminosity at 14–150 keV (C. Ricci et al. 2017), (8) Star formation rate (K. Ichikawa et al. 2017, 2019), (9) Black hole mass (M. J. Koss et al. 2022), and (10) Column density (C. Ricci et al. 2017).

observations of the innermost regions of high-luminosity AGNs, which will exclude contamination from the host galaxy. Thanks to ALMA's unmatched resolution and sensitivity, it is now possible to detect nuclear millimeter emission on scales of <400 pc for AGNs at $z < 0.16$.

In this manuscript, we investigate the relationship between millimeter emission and X-ray, optical/UV, and bolometric output for SMBHs accreting more rapidly than those studied by R23. The AGNs in our sample exhibit higher bolometric corrections ($\kappa_{2-10} = 29$–194), higher Eddington ratios ($\lambda_{\rm Edd} = 0.19$–0.85), and larger bolometric luminosities ($\log(L_{\rm bol}/{\rm erg\ s^{-1}}) = 45.3$–46.3). To study these sources, we obtained new quasi-simultaneous observations with ALMA at 100 GHz and with Swift at 2–10 keV. This data will allow us to test whether the tight millimeter/X-ray correlation reported by R23 extends to more luminous AGNs, or if these sources deviate from the relation. While it is known that the X-ray fraction decreases in higher-luminosity AGNs, reflected by the rising $\kappa_{\rm X}$, it remains unclear how the millimeter emission behaves and how this relation might evolve. The correlation derived in this work could, in the future, be used to probe the innermost regions of luminous, heavily obscured AGNs that are otherwise hidden from X-ray surveys.

This paper is structured as follows: Section 2 presents the sample of AGNs used in this work and describes the observations with ALMA and Swift. Section 3 describes the data reduction and imaging procedures, as well as the methods used to measure the flux densities for each source. Section 4 presents the resulting relations between millimeter and X-ray, optical/UV, and bolometric emission. Section 5 discusses what processes might explain the relations we observe. Finally, our conclusions are presented in Section 6.

In this paper, we adopt the standard cosmological parameters ($H_0 = 70\,{\rm km\,s^{-1}\,Mpc^{-1}}$, $\Omega_{\rm m} = 0.3$, and $\Omega_\Lambda = 0.7$). The correlations in this work were obtained using the STATISTICS module[24] from the Python SCIPY library (P. Virtanen et al. 2020). We present correlations in the luminosity domain rather than flux space, since T. Isobe et al. (1986) demonstrated that luminosity relations are more appropriate for recovering intrinsic physical correlations. When evaluating the significance of a correlation, we adopt the Spearman–r correlation test where a p-value <0.01 indicates a significant correlation. Finally, all uncertainties presented are 1σ unless stated otherwise.

2. Sample and Observations

We obtained quasi-simultaneous observations with ALMA at 100 GHz and with Swift in the X-ray and UV bands of nine nearby ($z = 0.058$–0.155) and unobscured AGNs. Details on the sample selection are presented in Section 2.1, and we provide a detailed discussion of the ALMA and Swift observations in Sections 2.2 and 2.3, respectively.

2.1. Sample Selection

Our nine targets were selected to have the highest bolometric luminosities in the all-sky Burst Alert Telescope (BAT) 70 month hard-X-ray survey[25] (W. H. Baumgartner et al. 2013) that are observable with ALMA.[26] BAT, which is on board the Neil Gehrels Swift Observatory, operates in the hard-X-ray band, covering energies between 14 keV and 195 keV. Throughout the BAT survey, more than 1000 nearby AGNs ($z < 0.1$) have been observed for 70 months (W. H. Baumgartner et al. 2013), including highly obscured AGNs that had not been detected before (C. Ricci et al. 2015). The BAT luminosities ($L_{14-150\,\rm keV}$) of the sources in our sample are presented in Table 1 and were taken from C. Ricci et al. (2017).

Additionally, these sources are RQ AGNs; thus, their radio-loudness values ($R_{\rm X}$) are all below the radio-quietness threshold of $R_{\rm X} = L_{1.4\,\rm GHz}/L_{14-195\,\rm keV} \leqslant -4.7$ (S. H. Teng et al. 2011). Their radio-loudness is also consistent with that of the lower-luminosity sample from R23, which has an average value of $\log R_{\rm X} = -5.31$, compared to $\log R_{\rm X} = -5.37$ for our sample.

Furthermore, our sources were selected to have higher bolometric luminosities, Eddington ratios, and bolometric corrections than the sample by R23. Recently, K. K. Gupta et al. (2024, hereafter G24) performed a thorough analysis on 236 hard-X-rays selected and nearby ($z < 0.3$) unobscured AGNs from the BAT AGN Spectroscopic Survey (BASS;[27]

---

[24] https://docs.scipy.org/doc/scipy/reference/stats.html

[25] https://swift.gsfc.nasa.gov/results/bs70mon/

[26] ALMA can only observe sources within source Declinations of −70 and +40; see https://almascience.eso.org/documents-and-tools/cycle10/alma-technical-handbook.

[27] https://www.bass-survey.com

M. Koss et al. 2017; C. Ricci et al. 2017; M. J. Koss et al. 2022) based on simultaneous optical to X-ray observations. BASS provided multiwavelength observations of the BAT AGNs and accurately measured AGN parameters such as $M_{\rm BH}$, $N_{\rm H}$, and intrinsic X-ray luminosities. Additionally, SFRs were obtained by fitting the IR spectral energy distribution (SED) of these AGNs (K. Ichikawa et al. 2017, 2019). G24 constructed broadband SEDs that were corrected for host galaxy contamination and, thereafter, obtained accurate values for important AGN parameters such as $L_{\rm bol}$, $\lambda_{\rm Edd}$, and $\kappa_{\rm X}$, upon which the sample selection criterion in this work is based.

A total of 10 sources from BASS met our criteria. However, one source (SWIFT J1255.0–2657) was not visible during the observing period of 2023 October. Therefore, nine targets were ultimately observed with ALMA. These nine sources were all detected with both ALMA and Swift; no targets were excluded on the basis of nondetections.

Our nine selected sources have, as aforementioned, higher bolometric luminosities ($\log(L_{\rm bol}/{\rm erg\ s^{-1}}) = 45.3$–$46.3$), higher bolometric corrections ($\kappa_{2-10} = 29$–194), and higher Eddington ratios ($\lambda_{\rm Edd} = 0.19$–0.85) compared to the AGN sample by R23, which we use as a comparison sample throughout this work. The specific parameter values for each source, as well as BAT IDs and values for $M_{\rm BH}$, SFR and $N_{\rm H}$, are listed in Table 1. The values for $M_{\rm BH}$ were taken from M. J. Koss et al. (2022). The SFR from K. Ichikawa et al. (2017, 2019) and Y. Díaz et al. (2026, in preparation). Finally, the $N_{\rm H}$ were taken from C. Ricci et al. (2017); all sources have $\log(N_{\rm H}/{\rm cm^{-2}}) < 22$, confirming they are unobscured.

2.2. The ALMA Observations

ALMA observations (Proposal ID 2023.1.01046.S; PI: C. Ricci) of our sample were carried out in Band 3, which covers frequencies from 84 GHz to 116 GHz, and were taken between 2023 October 1 and October 26, with configuration C–8. The spectral configuration of the ALMA observations consisted of four spectral windows (SPWs) divided into 128 channels (0.01563 GHz wide), with central frequencies of 90.52 GHz, 92.48 GHz, 102.52 GHz, and 104.48 GHz, respectively. These four SPWs were combined to map the continuum. Furthermore, a standard calibration strategy was adopted: a single bright quasar was used as both the flux and bandpass calibrator, while a second quasar was used as a phase calibrator. Details about these observations are reported in Table 2.

2.3. The Swift Observations

The Swift/X-Ray Telescope (XRT; D. N. Burrows et al. 2005) operates in the X-ray band, ranging between energies of 0.3–10 keV. From the XRT observations of our sources (PI: C. Ricci), seven out of nine observations were obtained between 2023 October 6 and October 17, to be quasi-simultaneous with the ALMA observations. However, observations of Mrk 813 and LEDA 126226 were obtained on 2023 December 12 and December 26, respectively, since they could not be observed before due to Sun constraints. All XRT observations were performed in Photon Counting mode. Observation dates and exposure times are listed in Table 3. Observation IDs are presented in Table 4 (Appendix B).

In addition to X-ray observations from the XRT, optical/UV observations were obtained with the Swift Ultraviolet/Optical Telescope (UVOT; T. S. Poole et al. 2008; A. A. Breeveld et al. 2010). UVOT can observe in six different filters, ranging between central wavelengths of 1928 Å (filter UVW2) and 5468 Å (filter V; T. S. Poole et al. 2008). Each source was observed using the Swift/UVOT filter that was available on the day of observation. The specific filters and the corresponding exposure times are listed in Table 3.

3. Data Reduction, Imaging, and Spectral Analysis

3.1. The Millimeter Data

The imaging and calibration of the ALMA data were performed with Common Astronomy Software Applications (CASA), version 6.5.4.9 (J. P. McMullin et al. 2007; CASA Team et al. 2022), and ALMA pipeline version 2023.1.0.124.

First, we created dirty images for the nine sources. The images of sources with multiple observations were combined, and from these images, the rms of the observation was obtained. This was done from regions in the image devoid of any emission. Furthermore, we visually inspected the individual SPWs to check for the presence of bright emission lines and found no evidence for line contamination in any of the sources. To obtain cleaned images, we used the CASA task `tclean` in multifrequency synthesis (mfs) mode with a cleaning threshold set to 1.5σ, which ensured that the residual images were free of any source emission. We used Briggs weighting and a robust[28] parameter of +0.5 to obtain the best trade-off between sensitivity and resolution. To ensure the images captured enough detail, we chose pixel sizes that satisfy the Nyquist sampling criterion. Finally, a mask was created around the source in the dirty image with the purpose of only cleaning the source emission. Images for each SPW were created together with images of all of the SPWs combined. We inspected the residuals to ensure sufficient cleaning with no residual flux. Then, the primary beam correction was applied. These primary beam corrected images and the respective beams and physical scales are displayed in Figure 5 (Appendix A.1). For each source, we obtained the peak flux density (S_ν), as the sources are predominantly unresolved. Furthermore, we adopted an uncertainty of $\sigma_{S^{\rm peak}_{\rm 100GHz}} = \sqrt{({\rm rms})^2 + (0.05 \times S^{\rm peak}_{\rm 100GHz})^2}$, where a 5% flux uncertainty agrees with the ALMA guidelines[29] for flux observations in Band 3. The resulting images had synthesized beam sizes in the range of $0\overset{''}{.}11$–$0\overset{''}{.}14$ (corresponding to physical scales of ~128–412 pc). The 1σ rms noise was in the range 6–14 μJy beam^{-1}. The angular resolutions achieved and the 1σ rms noise levels for each target are listed in Table 2.

Although not all sources are completely unresolved, as shown in Figure 5 (Appendix A.1), our focus is on the nuclear millimeter emission. Therefore, we use the peak flux density rather than the integrated flux. For eight sources, the peak-to-integrated flux ratio ranges between 0.80 and 1.14, with most values close to unity, indicating predominantly unresolved nuclear emission. The main outlier is LEDA 12773 with a ratio

---

[28] The CASA robust parameter controls the visibility weighting scheme used during imaging. It ranges between −2 and +2. At −2, uniform weighting prioritizes resolution, while at +2, natural weighting prioritizes sensitivity. A value of +0.5 is commonly used as the best trade-off between the two types of weighting.

[29] The flux density uncertainties can be found in the ALMA Cycle 10 Technical Handbook (https://almascience.eso.org/documents-and-tools/cycle10/alma-technical-handbook).

Table 2
Details on the ALMA Observations and Data

(1) Source	(2) Date (yyyy-mm-dd)	(3) Exposure (minutes)	(4) rms (μJy beam^{-1})	(5) θ (arcsec)	(6) $\theta_{\rm pc}$ (pc)	(7) $S_{\rm 100GHz}^{\rm peak}$ (mJy beam^{-1})	(8) $\log(\nu F_{\rm 100GHz})$ (erg s^{-1} cm^{-2})	(9) $\log(\nu L_{\rm 100GHz})$ (erg s^{-1})	(10) $\alpha_{\rm mm}$
Q 0119−286	2023-10-02	85.9	6.3	0.112	270	0.08 ± 0.01	−16.1	39.4	0.16 ± 0.85
PG 0026+129	2023-10-26	49.9	8.5	0.129	381	1.32 ± 0.07	−14.9	40.9	0.22 ± 0.35
PG 0052+251	2023-10-01	47.8	10.9	0.128	412	0.41 ± 0.02	−15.4	40.4	0.92 ± 0.35
Mrk 813	2023-10-10	26.3	13.4	0.123	281	0.38 ± 0.02	−15.4	40.1	0.89 ± 0.50
RHS 61	2023-10-02	64.1	8.6	0.139	347	0.59 ± 0.03	−15.2	40.3	0.28 ± 0.35
LEDA 126226	2023-10-09	25.7	13.8	0.105	214	2.74 ± 0.14	−14.6	40.8	0.48 ± 0.35
2MASX J022 23523+2508143	2023-10-01	31.8	12.3	0.127	158	0.71 ± 0.04	−15.1	39.8	1.41 ± 0.35
2MASX J173 11341+1442561	2023-10-10	111.3	6.3	0.135	224	0.12 ± 0.01	−15.9	39.3	0.15 ± 0.69
LEDA 12773	2023-10-01	82.9	6.7	0.106	128	0.19 ± 0.01	−15.7	39.2	0.37 ± 1.15

Note. (1) Source names, (2) Date of the observation, (3) Exposure time of the ALMA observations, (4) The rms of the observation, (5) The geometric mean resolution in arcseconds, (6) The obtained geometric mean resolution in parsecs, (7) Peak flux density, (8) Flux density at 100 GHz, (9) Luminosity at 100 GHz, and (10) Spectral index obtained from the four SPWs. For further details, see Section 3.1.

Table 3
Details on the Swift Observations and Data

	XRT				UVOT			
(1) Source	(2) Date (yyyy-mm-dd)	(3) Exposure (s)	(4) $\log(F_{2-10\,\mathrm{keV}})$ (erg s^{-1} cm^{-2})	(5) $\log(L_{2-10\,\mathrm{keV}})$ (erg s^{-1})	(6) Exposure Time (s)	(7) Filter and $\lambda_{\mathrm{center}}$ (Å)	$\log(\nu F_{\mathrm{UV}})$ (erg s^{-1} cm^{-2})	$\log(\nu L_{\mathrm{UV}})$ (erg s^{-1})
Q 0119−286	2023-10-06	1452	−12.0	43.5	1451	W1 / 2600	−11.0	44.6
PG 0026+129	2023-10-11	712	−11.2	44.5	710	U / 3465	−11.1	44.6
PG 0052+251	2023-10-06	1519	−11.1	44.7	1517	W1 / 2600	−11.0	44.8
Mrk 813	2023-12-01	1968	−11.4	44.1	1556, 394	M2 / 2246	−11.2	44.2
RHS 61	2023-10-07	1617	−11.1	44.4	…	…	…	…
LEDA 126226	2023-12-16	2023	−11.0	44.4	1497, 524	M2 / 2246	−10.9	44.5
2MASX J022 23523 +2508143	2023-10-07	1380	−11.4	43.6	1382	U / 3465	−10.8	44.2
2MASX J173 11341 +1442561	2023-10-11	1667	−11.6	43.6	1666	U / 3465	−11.3	43.9
LEDA 12773	2023-10-12	1499	−11.4	43.5	932, 198, 152	W2 / 1928	−11.2	43.8

Note. (1) Source names, (2) Date of the observations, (3) Exposure time of the XRT observations, (4) Intrinsic flux at 2–10 keV, (5) Intrinsic luminosity at 2–10 keV, (6) Exposure time of UVOT observations, (7) Filter and central wavelength of the UVOT filter used, (8) Intrinsic UV flux of the AGN, and (9) Intrinsic UV luminosity of the AGN. For further details, see Section 3.2.

of 0.65. Its ALMA image (Figure 5(i)) reveals a secondary component at $\sim 0\overset{\prime\prime}{.}08$ ($\sim$101 pc) from the nucleus, detected at a 7σ significance compared to the nuclear peak at 28σ. To further investigate this secondary component, we re-imaged LEDA 12773 using natural weighting (`robust = 2`) to maximize sensitivity to extended emission. The source appears unresolved at this weighting, suggesting the secondary component is compact and only marginally resolved at `robust = +0.5`. No archival high-resolution observations of this source are available for comparison. Future observations will be needed to determine the nature of this feature.

In addition to determining the flux densities of our sample, we computed the intraband spectral indices (α_{mm}), which are defined by the power-law relation $\log(S_\nu) = \alpha_{\mathrm{mm}} \log(\nu) + b$. We derive α_{mm} for each of our nine sources by measuring the peak flux densities across all four available SPWs and fitting the aforementioned power-law relation. Uncertainties on the values of α_{mm} were determined by centering the fit at $\nu = 100$ GHz to reduce the correlation between α_{mm} and b to better reflect the actual dispersion of the data and the uncertainties. The spectral indices for each source can be found in Table 2, while the resulting SEDs can be found in Figure 6 (Appendix A.2). We find a range of spectral indices between $\alpha_{\mathrm{mm}} = 0.15 \pm 0.69$ and $\alpha_{\mathrm{mm}} = 1.41 \pm 0.35$, with an average of $\alpha_{\mathrm{mm}}^{\mathrm{av}} = 0.55 \pm 0.15$. This is consistent with the average spectral index of $\alpha_{230\mathrm{GHz}}^{\mathrm{av}} = 0.5 \pm 1.2$ at 230 GHz reported by T. Kawamuro et al. (2023). However, the derived spectral indices in this work are subject to large uncertainties, as the four SPWs span only a narrow frequency range and are prone to scatter. Broadband observations are needed to confidently constrain the spectral slopes in these sources.

3.2. The X-Ray Data

Spectral analysis of the X-ray observations was performed with XSPEC version 12.14.0h (K. A. Arnaud 1996) and using XRTPIPELINE following the standard guidelines (P. A. Evans et al. 2009). The XRT data cover energies between 0.3 and 10 keV. For this work, we used flux densities and luminosities in the 2–10 keV range to mitigate the effects of absorption. We binned the spectra at a minimum of one count per energy bin over the whole energy range and subtracted the background. For the spectral fit, we fitted the XRT data to the power-law model `ZPOW` including `TBABS` to account for Galactic absorption in the direction of the sources (J. Wilms et al. 2000). The parameters for this model are z, the photon index (Γ), and the Galactic absorption[30] ($N_{\mathrm{H,Gal}}$), which we fixed to the values presented in Table 4 (Appendix B). Cash statistics (C-stat; W. Cash 1979) was applied to the XRT data because of the low number of counts in the data. The values of Γ resulting from the fit are listed in Table 4 (Appendix B), along with their 90% confidence uncertainties.

Eight out of nine sources were fitted with this model. However, for the source 2MASX J02223523+2508143, we found evidence for the presence of an absorber. Therefore, we fitted an additional absorber component using `ZXIPCF` (J. Reeves et al. 2008). The presence of this absorber is further discussed in Appendix C.5.

To determine the quality of the fits, we calculated the ratio between C-stat and the degrees of freedom (dof). For eight sources, the ratios range from 0.8–1, as shown in Table 4, indicating generally acceptable fits. One source, Q 0119–286, stands out as an outlier with a lower ratio of 0.6, presumably due to the low number of counts (39) in the observation.

From these spectral fits, we obtain the intrinsic fluxes in the 2–10 keV band, and we determined the luminosities including a k-correction, which accounts for redshifting effects. This was done using the following relation:

$$L_{2-10\,\mathrm{keV}} = 4\pi D_L^2 \frac{F_{2-10\,\mathrm{keV}}}{(1+z)^{2-\Gamma}}, \tag{1}$$

where D_L is the luminosity distance. Because the X-ray spectrum of the source 2MASX J02223523+2508143 is affected by an absorber, the observed luminosity underestimates

---

[30] The values for the Galactic absorption were obtained from the HEASARC $N_{\mathrm{H,Gal}}$ calculator (https://heasarc.gsfc.nasa.gov/cgi-bin/Tools/w3nh/w3nh.pl)

the intrinsic emission; we therefore compute the unabsorbed luminosity with `XSPEC` to recover the true AGN power.

The intrinsic X-ray flux densities and luminosities are presented in Table 3. The broadband X-ray spectra and our best fits can be found in Figure 7 (Appendix B.1).

3.3. The UV Data

For the UV data, we followed the data reduction procedure recommended by the Swift/UVOT Software Guide Version 2.2[31] and the procedure described by G24. Each source was observed in a single filter, as listed in Table 3, except for RHS 61, which was not observed by UVOT.

From the raw UVOT images, we produced calibrated sky images to derive magnitudes and, subsequently, the fluxes of our sources. Using the latest UVOT CALDB calibration files, available at 2024 February 1,[32] we generated bad pixel maps with `uvotbadpix` and applied flat-field corrections using `uvotflatfield` along with the CALDB file. These corrections were then applied to the raw images to produce the final sky images and obtain the UV flux densities.

Mrk 813, LEDA 126226, and LEDA 12773 consisted of two, two, and three separate observations, respectively. These were stacked to obtain deeper images, after which the UV flux density was determined from the final sky image. However, before stacking the images, any misalignment between the separate observations had to be corrected for with `uvotimsum`. This was achieved by aligning known reference points within the images. This aspect correction, performed using `uvotskycorr`, was successful for LEDA 12773, which enabled the stacking of the three exposures. The resulting image was visually inspected to determine whether the source was indeed aligned. For Mrk 813, one of the two exposures lacked sufficient detections, making aspect correction impossible. Consequently, we proceeded with the single exposure that had enough detections. Similarly, for LEDA 126226, the image with the longest exposure time was used as the final sky image, since the aspect correction could not be performed.

To obtain the magnitudes (m) and background noise from the final sky images, we defined regions with a radius of 5″ around the source and 20″ for the background. The magnitudes were then determined using `uvotsource`, and fluxes were calculated using the relation:

$$m - m_0 = -2.5\log(F\,[\text{counts}]), \tag{2}$$

where the zero-point magnitude (m_0) differed for each filter. This formula produced a flux in count units, which was then converted to mJy using a conversion factor.[33] All magnitudes are presented in Table 4 (Appendix B).

The measured UV fluxes include contributions from both the AGN and the host galaxy, with the latter expected to remain constant over time. Therefore, the flux from the host galaxy was subtracted. We used host galaxy fluxes calculated by G24, who obtained these values for our sources using `GALFIT` (C. Y. Peng et al. 2002, 2010). Finally, the intrinsic AGN flux was obtained by correcting the observed flux for dust extinction from both the host galaxy, characterized by $E(B-V)_{\rm HG}$, and the Milky Way, characterized by a reddening constant of $R_V = 3.08$ (Y. C. Pei 1992). Additionally, we accounted for the wavelength-dependent variation of extinction, as described by the extinction curve $k(\lambda)$. The values of $E(B-V)_{\rm HG}$ and $k(\lambda)$ for each source and UVOT filter were determined by G24 through broadband SED fitting. These values are presented in Table 4 (Appendix B). We used these corrections to obtain the intrinsic flux as follows:

$$F_{\rm AGN,intr} = F_{\rm AGN,obs} \times 10^{\,0.4\,R_V\,E(B-V)\,k(\lambda)}. \tag{3}$$

The final intrinsic UV luminosities are listed in Table 3.

4. Results

Here, we present the observations of the nine AGNs with higher bolometric luminosities, Eddington ratios, and bolometric corrections to investigate the millimeter/X-ray relation. In this work, we compare our sample to the lower-luminosity sample of R23. For an accurate comparison, we will express some of our results in terms of the ratio between the millimeter and X-ray luminosity ($\nu L_{100\rm GHz}/L_{2-10\rm keV}$).

4.1. The Millimeter versus X-Ray Relation

Figure 1 presents the relation between the 100 GHz emission and the intrinsic 2–10 keV emission for our nine sources and the sample by R23. Since the ALMA and Swift/XRT observations were obtained quasi-simultaneously, while the Swift/BAT fluxes are time-averaged over several years, we adopt the 2–10 keV band for the X-ray luminosities rather than the 14–150 keV band, although both are reported by R23. To compare our results with R23, we converted their 14–150 keV fluxes into the 2–10 keV band by assuming a photon index of $\Gamma = 1.8$, which is the median value found for nearby AGNs by C. Ricci et al. (2017). This also minimizes the effects of absorption, which affect more strongly at $E < 20$ keV.

Figure 1 shows that the high-luminosity AGNs deviate from the linear correlation obtained by R23. Therefore, we computed the new relation between millimeter and X-ray emission over the full available range of X-ray luminosities $\log(L_{2-10\rm keV}/\text{erg s}^{-1}) = 41$–45. We fitted a second-degree polynomial and obtained the relation:

$$\log\left(\frac{L_{100\,\rm GHz}}{10^{38}\ \text{erg s}^{-1}}\right) = (0.15 \pm 0.05)\log\left(\frac{L_{2-10\,\rm keV}}{10^{43}\ \text{erg s}^{-1}}\right)^2 + (1.20 \pm 0.05)\log\left(\frac{L_{2-10\,\rm keV}}{10^{43}\ \text{erg s}^{-1}}\right) \tag{4}$$

$$+(0.54 \pm 0.07), \tag{5}$$

with a p-value of 1.2×10^{-19} and an intrinsic 1σ scatter of 0.28 dex. When considering only the high-luminosity AGN, we find a slightly larger intrinsic scatter of 0.33 dex. We emphasize that the second-degree polynomial fit is intended as a phenomenological description of the combined dataset, rather than a physically motivated model. The key result is the systematic deviation of the high-luminosity sources from the linear relation defined for the low-luminosity AGN.

In addition to the 100 GHz versus 2–10 keV emission relation, we investigated the potential relation with the 0.3–2 keV range. This was done only for the unobscured AGNs in both samples, to avoid the strong effect of absorption in that energy range.

---

[31] https://swift.gsfc.nasa.gov/analysis/UVOT_swguide_v2_2.pdf

[32] https://heasarc.gsfc.nasa.gov/docs/heasarc/caldb/data/swift/uvota/index.html

[33] For the zero-point magnitudes (m_0) and conversion factors for each UVOT filter see https://swift.gsfc.nasa.gov/caldb/docs/uvot/uvot_caldb_AB_10wa.pdf.

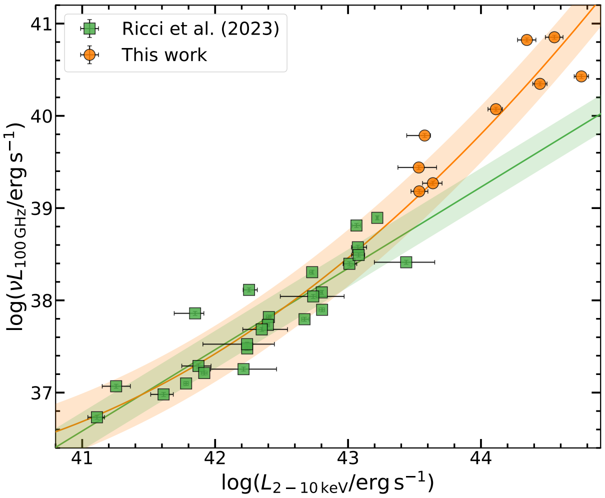

Figure 1. The 100 GHz vs. 2–10 keV emission for the AGN sample in this work (orange circles) and in R23 (green squares). We have fitted a second-degree polynomial relation between the millimeter and X-ray emission, as presented in Equation (5). This relation has a p-value of 2×10^{-19} and an intrinsic scatter of 0.28 dex.

These results can be found in Figure 8 (Appendix C.1). The 100 GHz emission appears to show a similar trend with the 0.3–2 keV band compared to the 2–10 keV emission, although with a larger scatter of 0.46 dex, which might be explained by the smaller sample size. Although the 14–150 keV luminosities listed in Table 1 are not simultaneous with our 100 GHz observations, we nonetheless present their relation in Figure 8 in Appendix C.2. We find a similar trend as seen for the 0.3–2 keV and 2–10 keV bands, with our high-luminosity sources generally deviating from the R23 relation, though the observed scatter may be partly attributable to the nonsimultaneity of the observations.

4.2. The Millimeter versus X-Ray Ratio

Figure 2 presents the millimeter/X-ray luminosity ratio ($\nu L_{100\mathrm{GHz}}/L_{2-10\mathrm{keV}}$) as a function of L_{bol}, λ_{Edd}, and κ_{2-10}.

In the left panel, for the nine sources in this work, L_{bol} values were taken from G24. To account for possible variability between the epochs of G24 and our new ALMA observations, these bolometric luminosities were re-normalized using the ratio of the UV fluxes measured in the two studies. One source, RHS 61, was not observed with Swift/UVOT and could therefore not be re-normalized; this source is marked with a star symbol in Figure 2. For the comparison sample of R23, bolometric luminosities were estimated as:

$$L_{\mathrm{bol}} = \kappa_{2-10} \times L_{2-10\mathrm{keV}}, \tag{6}$$

assuming a constant $\kappa_{2-10} = 20$ (R. V. Vasudevan & A. C. Fabian 2009). However, for six sources, G24 provided updated values of L_{bol} and λ_{Edd} based on source-specific κ_{2-10} values derived from simultaneous optical/UV/X-ray SED fitting. The method used to estimate L_{bol} for each source in the sample by R23 is indicated in the figure.

The middle panel shows the millimeter/X-ray luminosity ratio as a function of λ_{Edd}. We adopt the λ_{Edd} values from G24 for both samples. ESO 138–1 is excluded from the R23 sample due to the large uncertainty in its black hole mass, with published estimates spanning 10^5–$10^7\,M_\odot$ (e.g., E. Piconcelli et al. 2011; F. C. Cerqueira-Campos et al. 2021; A. Rodríguez-Ardila et al. 2024).

The right panel presents the millimeter/X-ray luminosity ratio as a function of κ_{2-10}. Since R23 assumed a constant $\kappa_{2-10} = 20$ for most sources, only sources for which G24 derived individual κ_{2-10} values from broadband SED fitting are included.

As shown in all panels of Figure 2, our sample exhibits systematically higher millimeter/X-ray luminosity ratios, with a mean of $-4.02^{+0.37}_{-0.33}$, compared to -4.58 ± 0.06 reported by R23. These averages are indicated by the orange dashed (this work) and green dotted (R23) lines, respectively. The two-sample Anderson–Darling test[34] (F. W. Scholz & M. A. Stephens 1987) yields $p < 0.001$, where p is the probability that the two samples are drawn from the same parent distribution. This further confirms that the two samples are indeed statistically distinct.

4.3. The Millimeter versus UV and Bolometric Emission

In addition to millimeter and X-ray observations, we have obtained UV observations. However, as described in Section 3.3, each source from our sample was observed with Swift/UVOT using a different filter. Since each filter traces a distinct part of the accretion disk emission, no observation represents the full disk emission. Therefore, it is not useful to directly compare the new UV observations among different sources and to search for a correlation with millimeter emission. To enable a consistent comparison with the millimeter, we instead consider the total disk emission ($\nu F_{\mathrm{UV,disk}}$) integrated over the range 10^{-7} to 0.1 keV as determined by G24. For our sources, we re-normalize this disk emission from G24 using the fluxes from the new UV observations to take variability into account.

Figure 3 presents the millimeter versus total disk emission. Here, we do not include RHS 61, since this source was not observed with UVOT. Furthermore, we only included the six sources from R23 for which optical/UV observations were reported by G24. Between the millimeter and disk luminosities, we obtain a linear correlation of the form:

$$\log(\nu L_{100\mathrm{GHz}}) = (0.76 \pm 0.08)\log(\nu L_{\mathrm{UV,disk}}) + (5.47 \pm 3.57), \tag{7}$$

with a p-value of 7×10^{-6}, suggesting a significant correlation, and a large intrinsic scatter of 0.45 dex.

Figure 3 also shows the relation between millimeter and bolometric emission, revealing a linear trend, though also accompanied by significant scatter. We obtain a linear relation of the form:

$$\log(\nu L_{100\mathrm{GHz}}) = (1.01 \pm 0.06)\log(L_{\mathrm{bol}}) - (6.22 \pm 2.54), \tag{8}$$

with a p-value of 1.5×10^{-15} and an intrinsic scatter of 0.35 dex. Given the linear relation observed between the millimeter and UV emission, the corresponding correlation with bolometric luminosity is unsurprising, as the bulk of the bolometric output is expected to emerge in the UV.

4.4. Robustness Checks

4.4.1. Physical Scale/Beam Size Effects

Since our sources lie at higher redshifts than those in R23, the same beam corresponds to larger physical scales in our

---

[34] We used the two-sample SCIPY.STATS.ANDERSON function from https://docs.scipy.org/doc/scipy/reference/generated/scipy.stats.anderson_ksamp.html#scipy.stats.anderson_ksamp

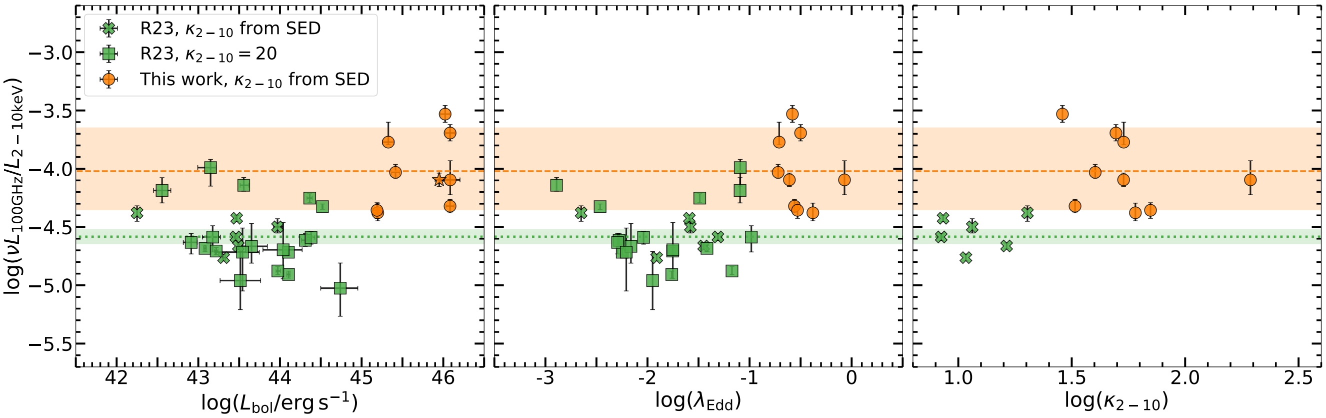

Figure 2. Ratio of the 100 GHz emission over the intrinsic 2–10 keV emission as a function of AGN parameters for the sources in this work (orange) and in R23 (green). Mean ratios are shown as dashed/dotted horizontal lines. Left: luminosity ratio vs. bolometric luminosity $L_{\rm bol}$. The bolometric luminosities for our sample were determined by G24 and normalized using UV observations from both this work and G24 to account for variability; RHS 61 was not normalized and is indicated with a star. For the R23 sample, bolometric luminosities were estimated either through $\kappa_{2-10} \times L_{2-10\rm keV}$ with $\kappa_{2-10} = 20$ (squares) or via SED fitting by G24 (crosses). Middle: luminosity ratio vs. Eddington ratio $\lambda_{\rm Edd}$. Right: luminosity ratio vs. bolometric correction κ_{2-10}.

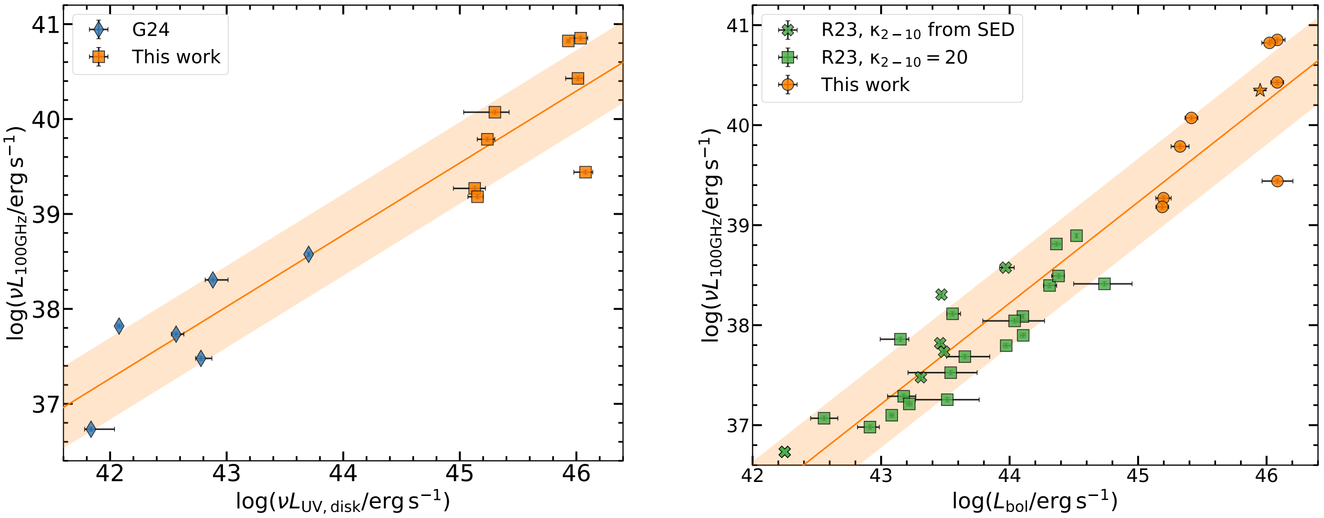

Figure 3. Left: the 100 GHz luminosity ($\nu L_{\rm 100GHz}$) vs. the optical/UV disk luminosity integrated over 10^{-7}–0.1 keV ($\nu L_{\rm UV,disk}$) for the sources in this work (orange squares). The disk emission was re-normalized using the new UVOT observations. The source RHS 61 is not shown, as it was not observed with UVOT. For comparison, six sources from R23 that were observed in the optical/UV by G24 are also included (blue diamond). We find a linear relation between the millimeter and UV emission, with a p-value of 7×10^{-6} and an intrinsic scatter of 0.45 dex. Right: the 100 GHz luminosity ($\nu L_{\rm 100GHz}$) vs. bolometric luminosity ($L_{\rm bol}$) for our sample and the sources from R23. Bolometric emission was estimated using $\kappa_{2-10} \times L_{2-10,\rm keV}$ with $\kappa_{2-10} = 20$ (squares) or from SED fitting by G24 (crosses). A linear fit to the millimeter/bolometric relation (Equation (8)) yields a correlation with a scatter of 0.35 dex.

observations. The physical scales explored in this research range from 128–412 pc, while R23 focused on scales <23 pc. This difference in scale could potentially lead to the observation of millimeter emission from outside of the nuclear region. Therefore, when stating that we observe higher millimeter/X-ray emission ratios in these highly luminous AGNs, we must confirm that we are not detecting additional millimeter emission from regions farther out.

The ALMA archive does not contain observations of the sources in the sample by R23 at physical scales comparable to ours, which would be needed to assess whether millimeter emission increases significantly at larger scales. Only data with beam sizes up to 3 times larger are currently available (C. S. Chang et al. 2026, in preparation), probing scales up to ∼50 pc. Furthermore, some of these sources show enhanced millimeter emission at larger scales while others do not, preventing a conclusive assessment. We will further discuss the potential contribution of larger-scale emission from star formation, which we suspect to be low, in Section 5.2.

In Figure 9 (Appendix C.3), we illustrate the millimeter/X-ray luminosity ratio versus the physical beam size ($\theta_{\rm pc}$) of our ALMA observations. We find that the ratio does not significantly increase with the beam size (p-value = 0.93), arguing against a dominant contribution from larger-scale emission. We note, however, that even in the absence of a trend, a small host galaxy contribution could still bias the normalization of the relation, particularly at high $L_{\rm bol}$ (i.e., a small host contribution would systematically shift the ratio upward for all sources). This possibility can be robustly tested with higher-resolution ALMA observations. Similarly, Figure 15 from T. Kawamuro et al. (2022) showed that the millimeter/X-ray luminosity ratio remains nearly constant across a wide range of physical resolutions (10 pc < $\theta_{\rm beam}$ < 220 pc) in their ALMA data. In particular, they found that the ratio at 230 GHz changes with physical resolution with a slope of only 7×10^{-4}. Based on this result, we do not expect the ratio to vary significantly when probing larger physical scales in our work compared to R23. Therefore, the extra millimeter emission expected at a larger beam of ∼412 pc would be small. Additionally, T. Kawamuro et al. (2022) determined that the nuclear millimeter emission dominated the observed emission in their observations at both high and low resolution. As a result, we anticipate that the contribution of diffuse emission, which does not originate from the nucleus, will be minimal.

However, based on these arguments, we cannot firmly establish whether the larger physical scales affect the measured level of millimeter emission. Future, higher spatial resolution studies will be needed to confirm this.

4.4.2. Rest-frame Frequency Effects

The millimeter observations in this work and in R23 were both obtained at an observed frequency of ∼100 GHz. However, due to the higher redshifts of our sources (z = 0.058–0.155) compared to those of R23 (z = 0.001–0.011), the corresponding rest-frame frequencies differ slightly. Since the millimeter spectra are approximately flat at these wavelengths (Section 3.1), this difference is expected to have minimal impact. But, to verify this, we compare the emission in overlapping SPWs from both studies: the second-highest frequency SPW at 102.5 GHz in R23 ($\nu_{\rm rest}$ = 102.6–103.7 GHz, depending on the redshift of the source) and the second-lowest frequency SPW in our data, centered at 92.5 GHz ($\nu_{\rm rest}$ = 97.8–106.8 GHz). This comparison shows that the flux ratios are consistent at similar rest-frame frequencies and are, on average, higher in our sample, confirming that the observed differences in millimeter/X-ray luminosity ratios are not due to rest-frequency effects.

5. Discussion

We have analyzed the millimeter/X-ray relation for nine high-luminosity AGNs and compared them with the R23 sample. Relative to that sample, our sources have higher $L_{\rm bol}$, $\lambda_{\rm Edd}$, and κ_{2-10}. As shown in Figure 1, our nine AGNs lie above the linear millimeter/X-ray correlation established by R23. Consequently, we derived a new second-degree polynomial relation, presented in Equation (5), spanning the full X-ray luminosity range explored ($\log(L_{2-10}/{\rm erg\ s^{-1}}) = 41.1$–44.8), with a scatter of 0.28 dex. Consistently, in Figure 2, we find, on average, higher millimeter/X-ray luminosity ratios for our sample. Turning to the comparison with disk emission (see Figure 3), we find a linear relation, although with substantial scatter (0.45 dex), which may be partly driven by the smaller sample size. Furthermore, when comparing millimeter and bolometric emission (see Figure 3), we observe a significant linear correlation as well, with a scatter of 0.35 dex.

In Sections 5.1 and 5.2, we will assess the millimeter origin by discussing the spectral index and examine whether the observed millimeter/X-ray luminosity ratios show any dependence on $M_{\rm BH}$ and SFR. This is particularly relevant for evaluating the reliability of millimeter emission as a tracer of AGN power, as discussed in Section 1. In Section 5.3, we will discuss in more detail the possible origins of the deviation of the high-luminosity sources from the relation established by R23, specifically addressing whether it might be driven by a relative decrease in X-ray emission (Section 5.3.1), or by a relative increase of the millimeter emission (Section 5.3.2). Finally, we will further study the origin of the millimeter emission through radio-to-submillimeter SEDs (Section 5.3.3).

5.1. Spectral Index α_{mm}

To determine the origin of the millimeter emission, we can investigate the spectral index ($\alpha_{\rm mm}$). The average spectral index of $\alpha_{\rm mm}^{\rm av} = 0.55 \pm 0.15$ (Section 3.1) is inconsistent with thermal dust emission, which follows a modified blackbody spectrum with $\alpha_{\rm dust} \approx -3.5$ (e.g., J. J. Condon et al. 1998; J. R. Mullaney et al. 2011), confirming that the observed millimeter emission is not dust-dominated.

The range of spectral indices observed across our sample ($0.15 \leqslant \alpha_{\rm mm} \leqslant 1.41$) is broadly consistent with a mixture of synchrotron and free–free processes. Negative spectral indices would suggest a contribution from optically thick synchrotron emission, for which self-absorption can produce $\alpha_{\rm synchr}^{\rm opt.thick} \approx -2.5$. Spectral indices in the range 0–0.5 are consistent with a combination of optically thin synchrotron emission ($\alpha_{\rm synchr}^{\rm opt.thin} \approx$ 0.5–1.0) and free–free emission ($\alpha_{\rm ff} \sim 0.1$; F. Panessa et al. 2019). Indices in the range 0.5–1.0 are most naturally explained by optically thin synchrotron emission. The steepest index in our sample ($\alpha_{\rm mm} = 1.41$) exceeds what is typically expected for optically thin synchrotron emission, though we caution that all spectral indices carry large uncertainties (up to $\sigma_{\alpha_{\rm mm}} \sim 1.15$) due to the narrow intraband frequency coverage of our ALMA observations (Section 3.1), limiting firm conclusions about the physical origin of the millimeter emission. The reliability of intraband $\alpha_{\rm mm}$ as a diagnostic tool will be further discussed in S. M. Venselaar et al. (2026, in preparation)

5.2. Dependence on M_{BH} and SFR

As discussed in Section 1, T. Kawamuro et al. (2022) and R23 found that the millimeter/X-ray luminosity ratio is independent of $M_{\rm BH}$ and SFR, implying that millimeter emission can serve as a proxy for X-ray emission across a wide range of these AGN parameters. To test whether this holds for our sample as well, we examined possible correlations between $\log(\nu L_{\rm 100GHz}/L_{\rm 2-10keV})$ and $M_{\rm BH}$ and SFR. This is especially important for the comparison with SFR, since there is the possibility that the larger scales we probe in this work include extra millimeter emission from star formation.

Figure 10 (Appendix C.4) shows the luminosity ratio versus $M_{\rm BH}$ and SFR. No significant correlation is observed between $\log(\nu L_{\rm 100GHz}/L_{\rm 2-10keV})$ and $M_{\rm BH}$, obtaining a p-value of 0.03. Although, it should be noted that the relation between $\nu L_{\rm 100GHz}/L_{\rm 2-10keV}$ and $M_{\rm BH}$ increases linearly if one does not consider data points at $\log(M_{\rm BH}/M_{\odot}) < 6.3$. However, it is expected that more luminous AGNs host more-massive SMBHs; therefore, in order to clearly assess any intrinsic dependence on $M_{\rm BH}$, we would need to compare sources with similar $L_{\rm bol}$ and $\lambda_{\rm Edd}$.

Furthermore, no significant correlation is observed between $\log(\nu L_{\rm 100GHz}/L_{\rm 2-10keV})$ and SFR, with a p-value of 0.22. Six of our nine AGNs have only upper limits for the SFR; therefore, to determine any correlation, we used Kendall's tau test to account for these upper limits (`pymccorrelation`; T. Isobe et al. 1986; P. A. Curran 2014; C. R. Harris et al. 2020; G. C. Privon et al. 2020; P. Virtanen et al. 2020). Two of the three objects for which SFRs could be inferred have higher values than the R23 sample. This may be attributed to the relatively large beam size of our observations and to the fact that more-massive systems tend to have higher SFRs, as expected from the galaxy main sequence (e.g., J. Brinchmann et al. 2004; K. G. Noeske et al. 2007).

5.3. Origin of the Millimeter/X-Ray Deviation for Luminous AGNs

In the following subsections, we discuss the origin of the higher millimeter/X-ray luminosity ratios in our sources compared to those reported by R23 (Figures 1 and 2). In particular, we address whether this offset might primarily be driven by a decrease in the X-ray emission (see Section 5.3.1) or an increase in the millimeter emission (see Section 5.3.2), and we employ SED modeling to further constrain the origin of the millimeter emission (see Section 5.3.3).

5.3.1. Relative Decrease in X-Ray Emission

We know that as $L_{\rm bol}$ increases, the absolute X-ray luminosity still rises, but its relative contribution to the total radiative output decreases, demonstrated by larger κ_{2-10} (e.g., E. Lusso et al. 2010; F. Duras et al. 2020; K. K. Gupta et al. 2024, 2025). This behavior has been linked to changes in the physical state of the corona at high luminosities (e.g., S. Martocchia et al. 2017; L. Zappacosta et al. 2020), although the underlying mechanisms remain uncertain. Consequently, the increased millimeter/X-ray ratios that we observe in this work might be due to this declining X-ray fraction at higher luminosities (Figures 1 and 2). At the same time, we find that the millimeter emission correlates linearly with $L_{\rm UV,disk}$ and $L_{\rm bol}$ (Figure 3), suggesting that the millimeter closely traces the total accretion power, while the X-rays start to deviate.

A physical interpretation for this behavior could be framed in terms of the coronal electron distribution. The hot corona likely consists of a dominant thermal population and a small nonthermal tail (e.g., A. C. Fabian et al. 2017). The thermal electrons are responsible for the X-ray emission, whereas the millimeter emission in RQ AGNs is thought to arise from the nonthermal component (e.g., Y. Inoue & A. Doi 2014). If the thermal electrons cool more efficiently at higher $L_{\rm bol}$, reducing the relative X-ray output as reflected in the rise of κ_{2-10}, while the nonthermal tail remains largely unaffected, the millimeter/X-ray ratio naturally increases. In this scenario, the nonthermal electrons continue to closely trace the bolometric output, explaining the observed linear $L_{\rm 100GHz}$–$L_{\rm bol}$ relation. This might raise the question of why cooling affects the two electron populations differently. A possible explanation is that the nonthermal electrons originate from a spatially extended region outside the compact X-ray corona, as proposed by A. M. Hankla et al. (2026).

Another commonly proposed explanation for the millimeter emission in RQ AGNs is a compact, low-power jet (e.g., F. Panessa et al. 2019). Based on our observations, it remains difficult to distinguish between a coronal and a jet origin for the millimeter emission. However, some studies have suggested that the compact jet and the corona might physically be the same structure (e.g., S. Markoff et al. 2005). Therefore, the nonthermal coronal electrons we propose as the source of the millimeter emission could also be associated with this compact jet. Recently, J. D. Paul & R. M. Plotkin (2026) tested this scenario for 69 RQ AGNs ($z < 0.2$), finding that compact jets could not account for the observed 5 GHz emission, and instead favor a coronal origin, with possible contributions from outflows in $\lambda_{\rm Edd}$ sources.

5.3.2. Relative Increase in Millimeter Emission

The AGNs in our sample have substantially higher Eddington ratios ($\lambda_{\rm Edd} = 0.19$–0.85) than those studied by R23 ($\lambda_{\rm Edd} = 10^{-3}$–$0.10$). High accretion rates are known to power stronger outflows; for example, F. Fiore et al. (2017) showed that mass outflow rates increase steeply with $L_{\rm bol}$. Such outflows can interact with the surrounding interstellar medium, producing shocks (e.g., J. Nims et al. 2015) that accelerate electrons in the ambient magnetic field and generate synchrotron emission (Y.-F. Jiang et al. 2010; H.-C. Hwang et al. 2018; T. Kawamuro et al. 2022). Consequently, additional millimeter emission could arise from outflow-induced shocks in our high-$\lambda_{\rm Edd}$ sources, potentially contributing to the enhanced millimeter/X-ray luminosity ratios we observe. Consistent with this picture, Figure 2 shows that the millimeter emission increases with both $L_{\rm bol}$ and $\lambda_{\rm Edd}$, suggesting that shock-related synchrotron emission may play a role in the observed trend.

Observational support for this scenario comes from the work of E. Shablovinskaia et al. (2025), who detected an unresolved, polarized source located ~20 pc from the nucleus of the RQ AGN NGC 3783 ($z \sim 0.009$). This source was part of the sample studied by R23 and exhibited the highest $L_{\rm 100GHz}$ among all sources. The polarized structure coincides with extended millimeter emission, contributing approximately 10% to the total millimeter flux, and aligns with a known narrow-line outflow previously detected with MUSE (M. den Brok et al. 2020) and GRAVITY (GRAVITY Collaboration et al. 2021). They concluded that the observed extended millimeter emission likely originates from an AGN-driven outflow, with the polarization resulting from synchrotron emission produced by shocks. Future work with ALMA polarimetry will investigate whether, for example, the extended millimeter emission observed in LEDA 12773 has a similar origin.

To further explore the potential link between millimeter emission and outflows in our sample, we analyzed archival high-quality X-ray spectra of our AGNs for signatures of ionized absorption (Appendix C.5.). We find that six of the nine AGNs have sufficiently high signal-to-noise X-ray observations for meaningful spectroscopic analysis, and in five of these six cases, we identified X-ray absorption features consistent with warm ionized outflows. Although this analysis is limited by small number statistics, the high incidence of X-ray outflows among sources with elevated millimeter/X-ray luminosity ratios might hint at a possible connection.

We also investigated potential correlations between $\alpha_{\rm mm}$ and $\lambda_{\rm Edd}$ or $L_{\rm bol}$, as presented in Figure 11 (Appendix C.6). Since more luminous AGNs are capable of driving stronger outflows, a correlation between $\alpha_{\rm mm}$ and $\lambda_{\rm Edd}$ or $L_{\rm bol}$ could indicate a contribution from outflow-related synchrotron emission. However, as shown in Figure 11 (Appendix C.6), no significant correlation is observed, with a p-value of 0.17 for $\alpha_{\rm mm}$ versus $\lambda_{\rm Edd}$ and a p-value of 0.37 for $\alpha_{\rm mm}$ versus $L_{\rm bol}$. This figure also includes the spectral indices for the sources from R23, which have an average value of $\alpha_{\rm mm}^{\rm av,R23} = 0.63 \pm 0.14$ (C. S. Chang et al. 2026, in preparation). The absence of a correlation between $\alpha_{\rm mm}$ and $\lambda_{\rm Edd}$ at ~230 GHz was previously reported by T. Kawamuro et al. (2022). These results suggest that, although outflows may contribute to the millimeter flux, they are unlikely to dominate the emission, which is instead primarily associated with the corona.

Supporting this conclusion, most of our sources exhibit relatively flat α_{mm} (Section 5.1), consistent with SSA in the corona. Such flat slopes are inconsistent with emission from outflow-driven shocks, which would produce steeper spectra (e.g., Y.-F. Jiang et al. 2010). Moreover, emission associated with AGN-driven outflows is generally expected to be most prominent at centimeter wavelengths rather than in the millimeter regime (e.g., T. Yamada et al. 2024). In line with this, J. D. Paul & R. M. Plotkin (2026) reported a radio excess at 5 GHz in RQ AGNs observed with the Karl G. Jansky Very Large Array (VLA) that appears to increase with λ_{Edd}, and which they suggested may originate from outflow-related synchrotron emission. A. M. Hankla et al. (2026) recently proposed a model in which millimeter emission could arise from an extended, outflowing region physically connected to the corona via magnetic fields, providing a mechanism for coronal-related millimeter emission beyond the compact corona. Notably, this coronal outflow was found to produce flat spectra, which agree with the values for α_{mm} we observe.

Finally, Figure 11 also presents α_{mm} versus SFR, where we do not observe any correlation either (p-value = 0.85). This supports that the millimeter emission is presumably not dominated by star formation from the larger physical scales probed in this work.

5.3.3. Radio to Submillimeter SED Modeling

To further investigate the origin of the millimeter emission we observe in our sample, we performed SED modeling. The radio to submillimeter SED of an RQ AGN could consist of several components, namely: (1) optically thin synchrotron emission from a diffuse population of relativistic electrons, (2) diffuse free–free emission from ionized gas, (3) synchrotron emission from a compact corona, and (4) thermal emission from dust. Of these, the most relevant at frequencies of ∼100 GHz is expected to be the corona, provided that the resolution of the observations is high enough to filter out most of the diffuse emission. However, in a more general case, one needs to account for all emission components in the SED. To achieve this, we use the SED fitting procedure presented by S. del Palacio et al. (2025). This method was originally tested in seven AGNs with $\lambda_{\mathrm{Edd}} \sim 0.003$–0.035, and it can allow us to infer coronal parameters for our sample. In particular, the corona synchrotron SED model mainly depends on two parameters: (i) the radius of the corona ($r_{\mathrm{c}} = R_{\mathrm{c}}/R_{\mathrm{g}}$, where $R_{\mathrm{g}} = GM_{\mathrm{BH}}/c^2$ is the gravitational radius) and (ii) the relativistic electron content, defined via the ratio (δ) between the energy density in nonthermal and thermal electrons. However, a well-sampled SED is required to disentangle the corona component in the SED and constrain these two main parameters.

For all of the objects in our sample, we looked for archival radio data. The archival data available for each source are described in Appendix C.7. The objects with the most complete radio to submillimeter SEDs are PG 0026+129 and PG 0052+251, for which extensive VLA (R. D. Baldi et al. 2022) and Very Long Baseline Array (VLBA; S. Chen et al. 2025) data exists. Additionally, ALMA Band 5 ($\nu_{\mathrm{center}} \sim 195$ GHz) observations are available for PG 0052+251 (Proposal ID 2023.1.01062.S; PI: F. Bauer). We show their SEDs and the fits in Figure 4. For the case of PG 0026+129, the fit yields well-constrained values of $r_{\mathrm{c}} = 217 \pm 13$ and $\log \delta = -1.06 \pm 0.11$, with a peak of the corona component at $\nu_{\mathrm{p}} = 120 \pm 10$ GHz and a flux $S_{\mathrm{p}} = 1.34 \pm 0.17$ mJy. Furthermore, a magnetic field strength (B) of $B \sim 19$ G was derived. The observed millimeter peak fluxes across the four SPWs range from 1.30 ± 0.06 to 1.34 ± 0.07 mJy, as shown in Figure 4. Therefore, this strongly supports the interpretation of the millimeter flux at ∼100 GHz coming almost exclusively from the corona. For PG 0052+251, the fit is more ambiguous, with possible contributions from free–free emission or diffuse synchrotron radiation. This demonstrates the need for multiband observations with similar resolutions. Nevertheless, we infer $\log \delta = -1.68^{+0.31}_{-1.17}$, a coronal size of $r_{\mathrm{c}} = 131 \pm 66$, a peak flux and frequency of $S_{\mathrm{p}} = 0.17 \pm 0.10$ mJy and $\nu_{\mathrm{p}} = 82 \pm 31$ GHz, respectively, and a magnetic field strength of $B \sim 12$ G. These coronal size values are consistent with those found for RQ AGNs by S. del Palacio et al. (2025), where the reported sizes ranged from $r_{\mathrm{c}} = 60$–250. For sources in our sample with sparse high-resolution archival data, it remains uncertain whether the 100 GHz emission originates entirely from the corona.

6. Conclusions

In this work, we studied a sample of nine RQ AGNs, which were selected for their high bolometric luminosities (L_{bol}), bolometric corrections ($\kappa_{2-10} = L_{\mathrm{bol}}/L_{2-10\mathrm{keV}}$), and Eddington ratios ($\lambda_{\mathrm{Edd}} = L_{\mathrm{bol}}/L_{\mathrm{Edd}}$) to investigate their millimeter/X-ray relation. These sources were chosen from the BAT hard-X-ray survey as the brightest AGNs that are observable with ALMA. For this study, we obtained new quasi-simultaneous observations with ALMA and Swift/XRT at 100 GHz and 2–10 keV, respectively.

1. We find that the high-luminosity AGNs with $\log(L_{\mathrm{bol}}/\mathrm{erg\ s^{-1}}) = 45.3$–46.3 are located above the millimeter/X-ray correlation that was obtained for lower-luminosity sources with $\log(L_{\mathrm{bol}}/\mathrm{erg\ s^{-1}}) < 45$ by R23 (Figures 1 and 2). We fit a second-degree polynomial to both samples (Equation (5)) and determine an intrinsic scatter of 0.28 dex. We obtain an average millimeter/X-ray luminosity ratio of $-4.02^{+0.37}_{-0.33}$, compared to a lower average ratio of -4.58 ± 0.06 for the less luminous AGNs (Sections 4.1 and 4.2).
2. We observe a linear relation between the millimeter and disk luminosities (Figure 3 and Equation (7) in Section 4.3), accompanied by a large intrinsic scatter of 0.45 dex. We find a significant linear relation between the millimeter and bolometric emission with a scatter of 0.35 dex (Figure 3 and Equation (8) in Section 4.3).
3. Since no clear correlation is observed between the millimeter/X-ray luminosity ratio and either black hole mass (M_{BH}) or SFR, we conclude that the millimeter/X-ray relation derived in this work might hold across a broad range of AGN properties (Section 5.2).
4. As L_{bol} rises, κ_{2-10} is known to increase. This declining X-ray fraction may drive the observed rise in the millimeter/X-ray ratio, while the millimeter emission continues to scale linearly with L_{bol}. The latter suggests that the millimeter emission traces the total accretion power and is largely insensitive to coronal changes. We propose that this behavior can be explained if the corona

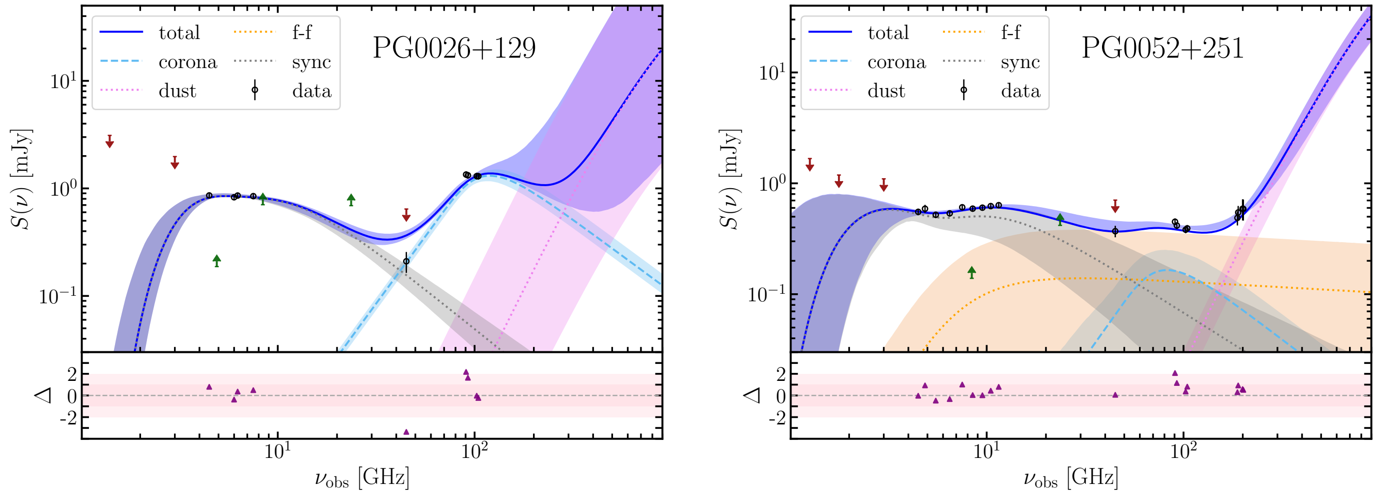

Figure 4. The best-constrained SEDs, including the new 100 GHz observations presented in this work and archival VLA, VLBA, and ALMA Band 5 ($\nu_{\rm center} \sim 195$ GHz) data. The separate components potentially contributing to the observed millimeter emission are indicated: millimeter emission from the corona, free–free emission, diffuse synchrotron emission, and dust.

hosts two electron populations: a thermal component that becomes less efficient at producing X-rays as $L_{\rm bol}$ rises, and a nonthermal population that continues to scale with the total accretion power (Section 5.3.1).

5. Another possibility is that the higher millimeter/X-ray ratios observed in our high-$\lambda_{\rm Edd}$ AGNs may be partly driven by an increase in millimeter emission associated with stronger outflows. Here, shock-induced synchrotron radiation can contribute to the millimeter flux, although the lack of a correlation between $\alpha_{\rm mm}$ and $\lambda_{\rm Edd}$ indicates that such outflow-related emission is likely a secondary component, with the corona remaining the dominant millimeter emitter (Section 5.3.2).
6. Furthermore, SED modeling for PG 0026+129 indicates that the millimeter emission is dominated by the corona. For PG 0052+251, a contribution of free–free or diffuse synchrotron emission is present as well. The size of the compact component is $R_{\rm c} \sim 130$–$220\,R_{\rm g}$, consistent with findings for other RQ AGNs. For the remaining sources, sparse high-resolution archival data or poorly constrained SEDs prevent robust determination of the coronal contribution.

In this work, we probe larger physical scales than the low-luminosity AGNs studied by R23. Despite this, the millimeter/X-ray luminosity ratio remains roughly constant with increasing scale. However, we cannot entirely rule out that the larger physical scales may influence the observed millimeter emission. Future observations will be essential for further constraining the exact contributions of the millimeter emission in high-luminosity RQ AGNs. The ALMA Wideband Sensitivity Upgrade (WSU), which will be implemented in the early 2030s, will allow for higher sensitivity observations and could decrease the significant uncertainties on, e.g., the millimeter spectral index $\alpha_{\rm mm}$. Additionally, higher-resolution observations will allow us to trace smaller physical scales in these sources, allowing for a more accurate comparison to the lower-luminosity sources from R23. Furthermore, millimeter polarimetry could shed light on the potential contribution of outflows to the observed millimeter emission, as was previously done by E. Shablovinskaia et al. (2025). This will be investigated in an accepted Cycle 12 ALMA proposal (Proposal ID 2025.1.00150.S; PI: S. Venselaar).

Acknowledgments

We thank the referee, Ehud Behar, and the AAS Statistics Editor for their helpful comments, which improved the quality of this work. We thank Brad Cenko and the Swift team for carrying out the observations of the sources in our sample.

S.V. acknowledges support from SNSF Consolidator grant F01−13252 and the China-Chile joint research fund. C.R. acknowledges support from SNSF Consolidator grant F01−13252, Fondecyt Regular grant 1230345, ANID BASAL project FB210003 and the China-Chile joint research fund. K.K.G. acknowledges financial support from the Belgian Federal Science Policy Office (BELSPO) in the framework of the PRODEX Programme of the European Space Agency. R.S. acknowledges funding from the CAS-ANID grant No. CAS220016. E.S. acknowledges a Humboldt Research Fellowship by the Alexander von Humboldt Foundation. E.T. acknowledges support from FONDECYT Regular 1250821.

This paper makes use of the following ALMA data: ADS/JAO.ALMA#2023.1.01046. ALMA is a partnership of ESO (representing its member states), NSF (USA), and NINS (Japan), together with NRC (Canada), MOST and ASIAA (Taiwan), and KASI (Republic of Korea), in cooperation with the Republic of Chile. The Joint ALMA Observatory is operated by ESO, AUI/NRAO, and NAOJ. The National Radio Astronomy Observatory and Green Bank Observatory are facilities of the U.S. National Science Foundation operated under cooperative agreement by Associated Universities, Inc.

Facilities: Swift, ALMA.

Appendix A
ALMA Data

A.1. Continuum Observations

We have obtained new ALMA observations of our sample of nine RQ AGNs. The observations and imaging of the observations are discussed in Section 2.2 and Section 3.1, respectively. The ALMA images obtained by our observations are displayed in Figure 5. Each image shows the beam in the bottom-left corner and the physical size of $0.''1$ in pc in the bottom-right corner.

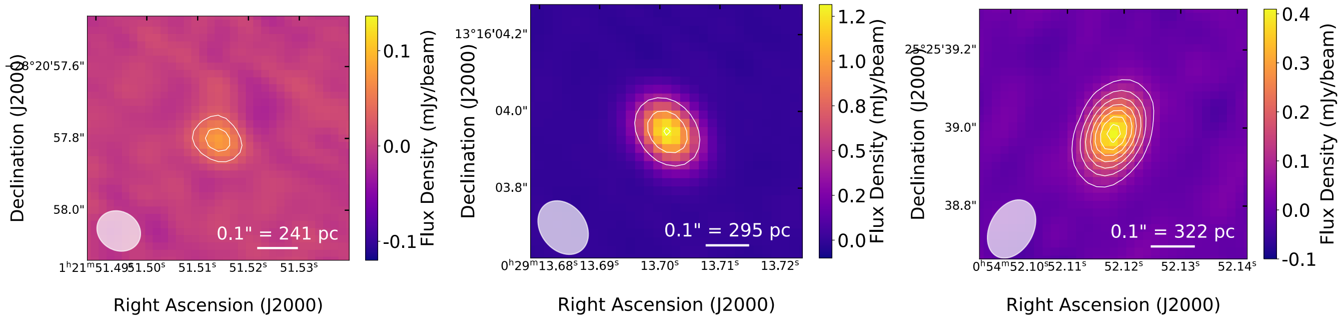

(a) Q 0119–286
Contours at 5σ and 10σ.

(b) PG 0026+129
Contours at 50σ, 100σ, 150σ.

(c) PG 0052+251
Contours from 5σ to 35σ.

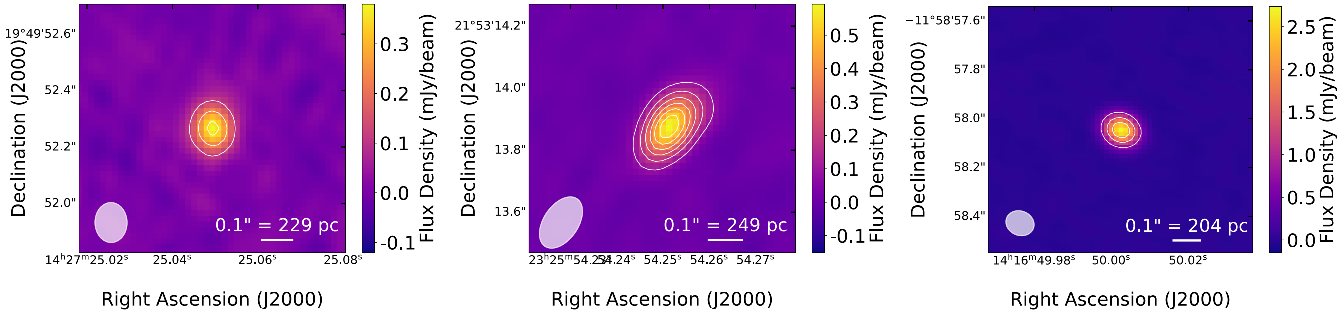

(d) Mrk 813
Contours at 5σ, 10σ, and 15σ.

(e) RHS 61
Contours from 10σ to 70σ.

(f) LEDA 12622
Contours at 50σ, 100σ, and 150σ.

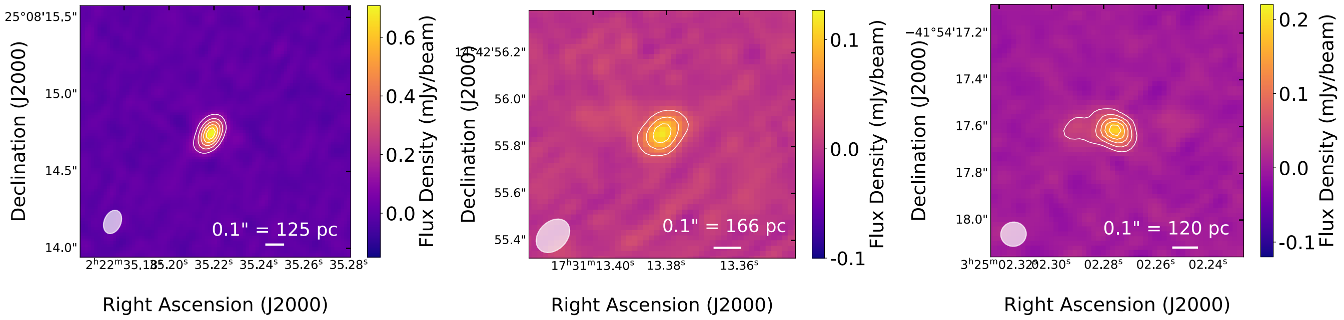

(g) 2MASX J02223523+2508143
Contours from 10σ to 50σ.

(h) 2MASX J17311341+1442561
Contours at 5σ, 10σ, and 15σ.

(i) LEDA 12773
Contours from 5σ to 25σ. The extra structure to the left peaks at 7σ.

Figure 5. ALMA observations of our nine high-luminosity AGNs. The beam sizes are displayed in the bottom-left corner. Furthermore, the bar in the bottom-right corner represents a scale of $0\overset{''}{.}1$ and the corresponding size in parsecs. Contours are displayed at multiples of σ as specified for each source. The respective values of σ and the beam size (θ) are listed in Table 2.

A.2. Spectral Index Determination

Figure 6 shows for each of our nine sources the resulting fit of $S_\nu \propto \nu^{-\alpha_{\rm mm}}$ to the peak fluxes in the four SPWs. The $\alpha_{\rm mm}$ values resulting from the fit are displayed in the figures as well.

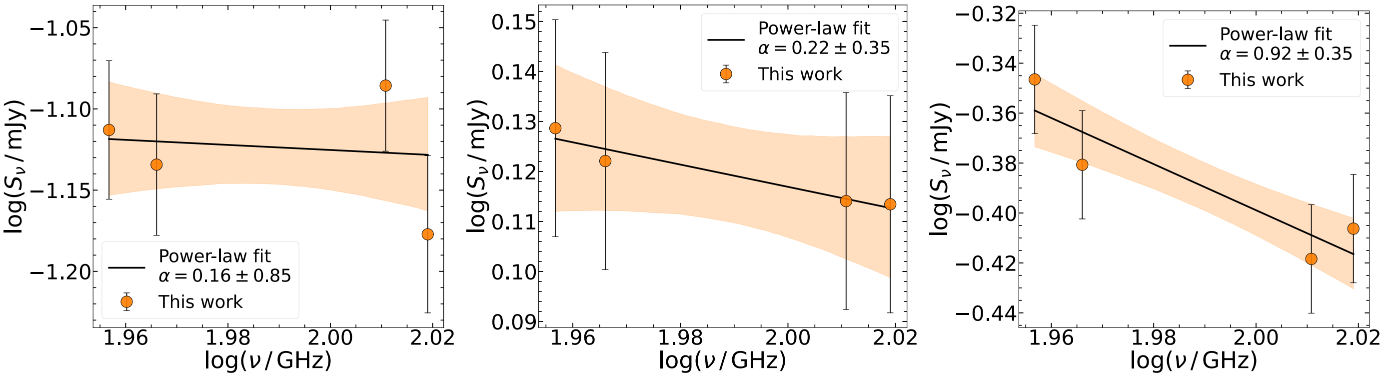

(a) Q 0119–286 **(b) PG 0026+129** **(c) PG 0052+251**

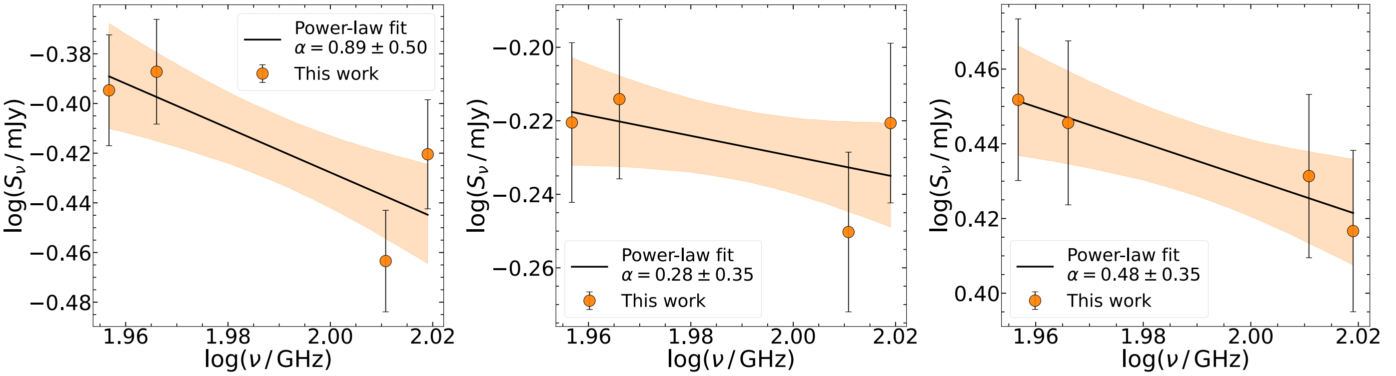

(d) Mrk 813 **(e) RHS 61** **(f) LEDA 12622**

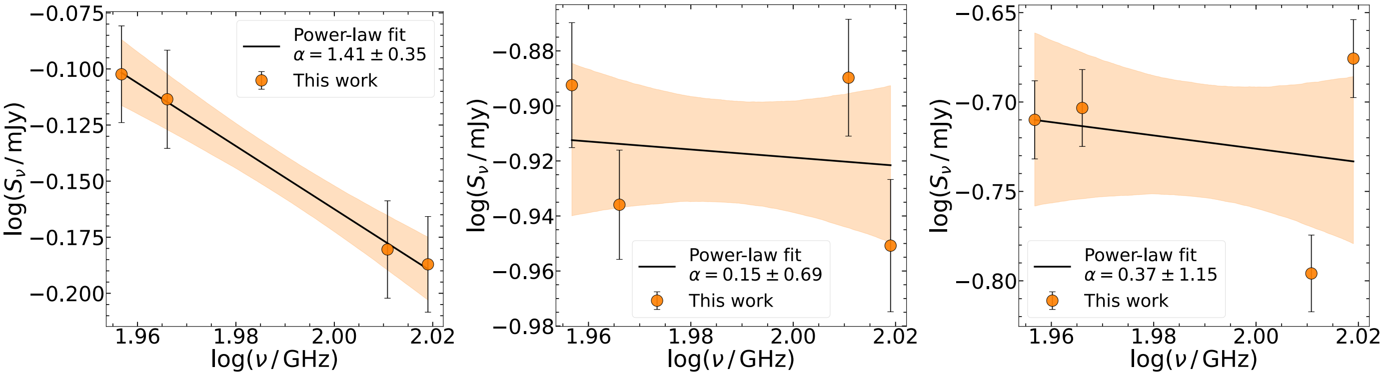

(g) 2MASX J02223523+2508143 **(h) 2MASX J17311341+1442561** **(i) LEDA 12773**

Figure 6. The fit of $S_{\rm mm} \propto \nu^{-\alpha_{\rm mm}}$ to the 100 GHz fluxes in mJy from the four separate SPWs for each of our sources. Systematic uncertainties on the 100 GHz fluxes are $\sigma_{S^{\rm peak}_{\rm 100GHz}} = \sqrt{({\rm rms})^2 + (0.05 \times S^{\rm peak}_{\rm 100GHz})^2}$ (see Section 3.1). The $\alpha_{\rm mm}$ values resulting from the fit, including the errors, are indicated in each figure.

Appendix B
Swift Data

We have obtained new Swift observations of our sample of nine RQ AGNs as well. The observations and images are discussed in Section 2.3 and Section 3.2, respectively.

Table 4 displays additional details on the XRT and UVOT data. We present for each source the Swift ID, the observation ID, the Galactic absorption column densities[35] ($N_{\rm H,Gal}$) as used in our X-ray spectral modeling and the photon index Γ derived from our spectral fits. We also provide the UV magnitudes, both including contributions from the host galaxy and AGN, and

---

[35] Obtained from the HEASARC $N_{\rm H,Gal}$ calculator: https://heasarc.gsfc.nasa.gov/cgi-bin/Tools/w3nh/w3nh.pl.

those corresponding to the host galaxy alone. As described in Section 3.3, we apply a correction factor for dust extinction.

We note that the source 2MASX J02223523+2508143 has a high correction factor of 45.0.

B.1. X-Ray Spectra

The X-ray spectra of our nine sources in the 2–10 keV range are displayed in Figure 7. The fitted model is described in Section 3.2, and the fitted parameters are presented in Table 4.

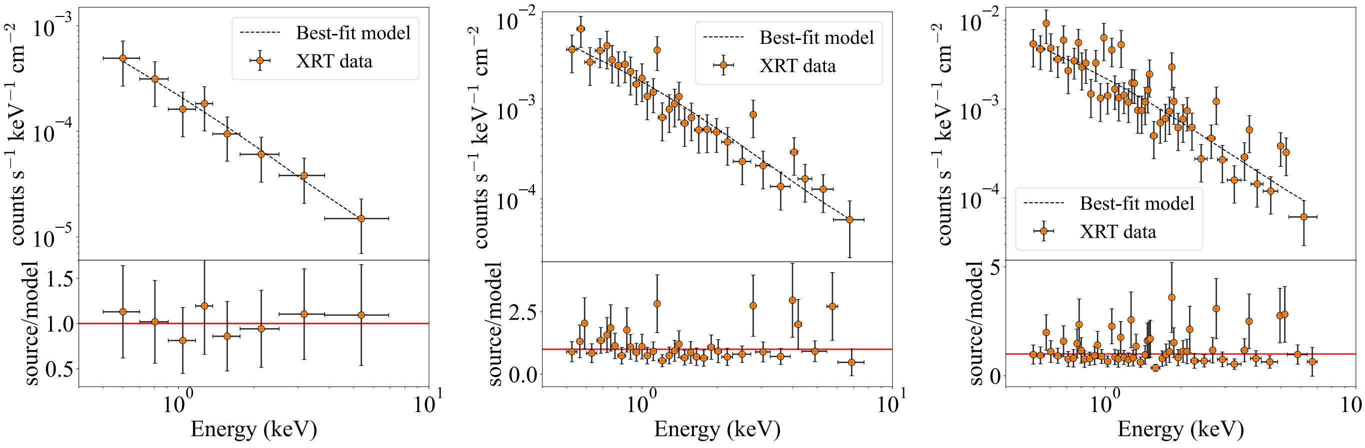

(a) Q 0119–286 **(b) PG 0026+129** **(c) PG 0052+251**

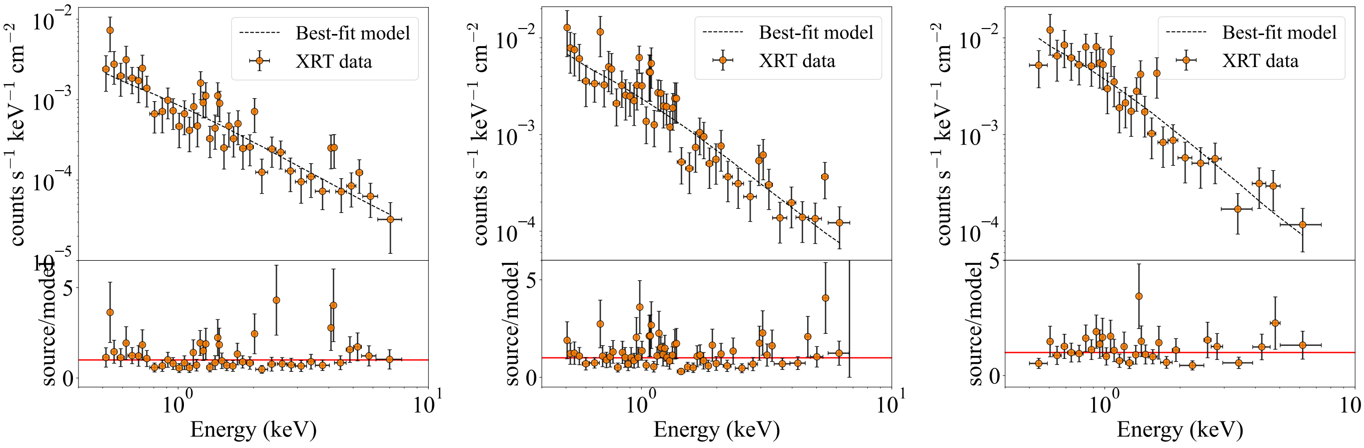

(d) Mrk 813 **(e) RHS 61** **(f) LEDA 12622**

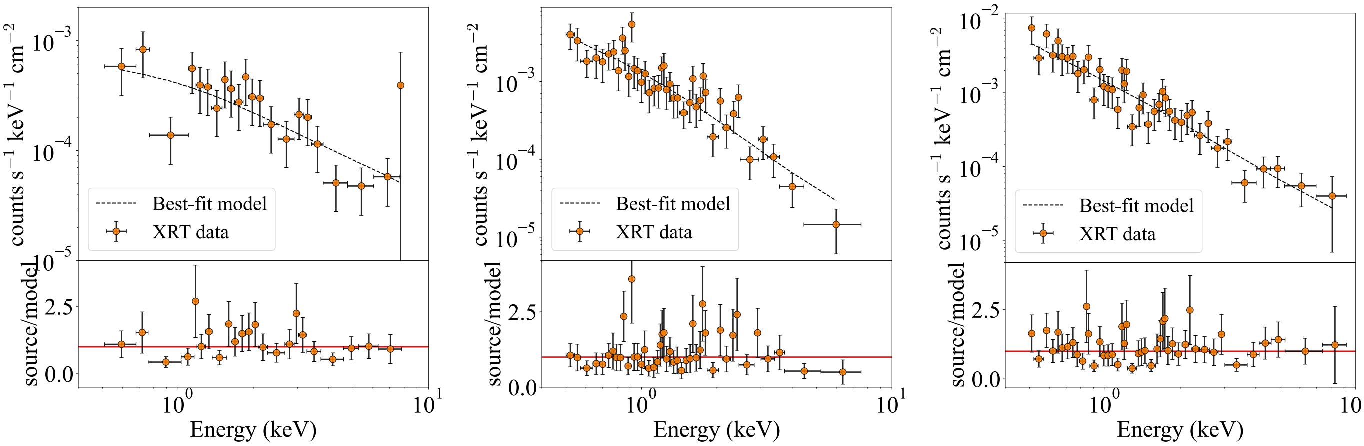

(g) 2MASX J02223523+2508143 **(h) 2MASX J17311341+1442561** **(i) LEDA 12773**

Figure 7. X-ray spectra of our nine sources at 2–10 keV. The top panel shows the spectra in counts. The bottom panel shows the ratio of the data and the fitted model.

Table 4
Additional Information on the Swift Data

			XRT			UVOT		
(1) Source	(2) SWIFT ID	(3) Observation ID	(4) $\log(N_{\rm H,Gal})$ (cm^{-2})	(5) Γ	(6) C-stat/dof	(7) $m_{\rm galaxy+AGN}$	(8) $m_{\rm galaxy}$	(9) Correction Factor
Q 0119−286	SWIFT J0122.0−2818	00045919010	20.2	1.7 ± 0.4	20/35	15.4	16.8	0.50
PG 0026+129	SWIFT J0029.2+1319	00037603004	20.7	2.0 ± 0.2	106/120	15.8	17.3	0.73
PG 0052+251	SWIFT J0054.9+2524	00037604006	20.6	1.8 ± 0.2	158/176	16.1	18.0	0.66
Mrk 813	SWIFT J1427.5+1949	00035307048	20.4	1.7 ± 0.2	133/163	16.0	16.8	0.59
RHS 61	SWIFT J2325.6+2157	00031323002	20.6	2.0 ± 0.2	165/161	…	…	…
LEDA 126226	SWIFT J1416.9−1158	00040708005	20.7	2.2 ± 0.2	92/118	15.5	18.4	0.42
2MASX J02223523+2508143	SWIFT J0222.3+2509	00032246003	20.8	1.7 ± 0.8	81/95	18.9	19.6	45.0
2MASX J17311341+1442561	SWIFT J1731.3+1442	00041781004	20.8	2.3 ± 0.2	112/145	16.6	19.9	0.77
LEDA 12773	SWIFT J0325.0−4154	00037556005	20.0	2.0 ± 0.2	122/153	16.6	18.6	0.69

Note. (1) Source names, (2) ID of the Swift observations, (3) Observation ID of the Swift observations, (4) Galactic absorption $N_{\rm H,Gal}$ in cm^{-2}, (5) Photon index obtained from the X-ray fits with their 90% confidence uncertainties, (6) Quality of the fit of the X-ray model expressed as the total fit statistics divided by the degrees of freedom, (7) The UV magnitude of the host galaxy and AGN combined, (8) UV magnitude of host galaxy, and (9) Correction factor for dust $10^{0.4R_V E(B-V) k(\lambda)}$.

Appendix C
Additional Tests on the Millimeter/X-Ray Relation

C.1. The 0.3–2 keV Energy Range

In addition to investigating the relation between the 2 and 10 keV and millimeter emission, we investigated the relation between 0.3 and 2 keV and millimeter emission, which is where the soft excess is located. Here, we have only adopted the sources from R23 that are unobscured. As can be seen in Figure 8, we observe a similar trend between the millimeter and 0.3–2 keV emission as with the millimeter and 2–10 keV emission. Again, we fitted a second-degree polynomial and obtained the relation:

$$\log\left(\frac{L_{100\,\rm GHz}}{10^{38}\,{\rm erg\,s^{-1}}}\right) = (0.17 \pm 0.09)\log\left(\frac{L_{0.3-2\,\rm keV}}{10^{43}\,{\rm erg\,s^{-1}}}\right)^2 + (1.21 \pm 0.12)\log\left(\frac{L_{0.3-2\,\rm keV}}{10^{43}\,{\rm erg\,s^{-1}}}\right) + (0.51 \pm 0.17), \quad (C1)$$

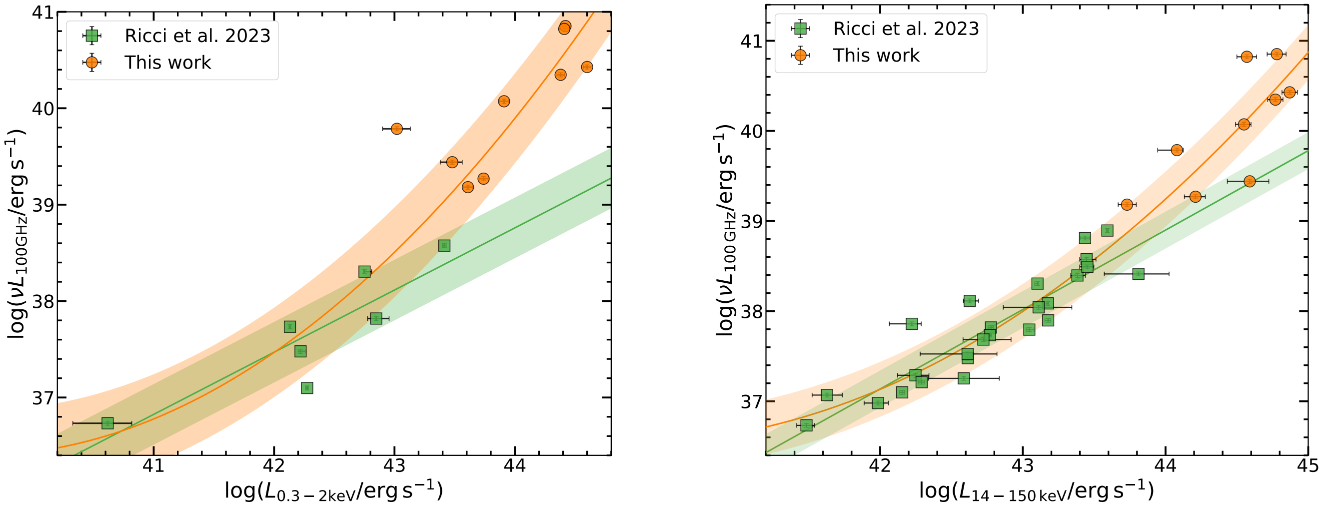

Figure 8. Left: the 100 GHz luminosity $\nu L_{\rm 100GHz}$ in erg s^{-1} vs. the intrinsic 0.3–2 keV luminosity $L_{\rm 0.3-2keV}$ in erg s^{-1} for sources by R23 and this work. We have fitted a second-degree polynomial relation to the millimeter and X-ray emission, presented in Equation (C1), which has an intrinsic scatter of 0.46 dex. Right: the 100 GHz luminosity $\nu L_{\rm 100GHz}$ in erg s^{-1} vs. the 14–150 keV luminosity $L_{\rm 14-150keV}$ in erg s^{-1}. We have fitted a second-degree polynomial, presented in Equation (C2), with an intrinsic scatter of 0.30 dex. The ALMA and Swift observations in this figure were not obtained simultaneously.

which has a large intrinsic scatter of 0.46 dex.

C.2. The 14–150 keV Energy Range

As discussed in Section 4.1, we adopt the 2–10 keV band rather than the 14–150 keV band also presented by R23, since the former was observed quasi-simultaneously with the ALMA data. Nevertheless, 14–150 keV luminosities are available from C. Ricci et al. (2017; also see Section 2.1), which are time-averaged over several years. Given the tight correlation reported by R23 between $L_{14-150\mathrm{keV}}$ and $L_{100\mathrm{GHz}}$, we show the corresponding relation for our sample in Figure 8, although with nonsimultaneous observations. We obtain the following second-degree polynomial relation:

$$\log\left(\frac{L_{100\ \mathrm{GHz}}}{10^{38}\ \mathrm{erg\ s^{-1}}}\right) = (0.19 \pm 0.06)\log\left(\frac{L_{14-150\ \mathrm{keV}}}{10^{43}\ \mathrm{erg\ s^{-1}}}\right)^2 + (1.06 \pm 0.07)\log\left(\frac{L_{14-150\ \mathrm{keV}}}{10^{43}\ \mathrm{erg\ s^{-1}}}\right) - (0.003 \pm 0.07), \quad (\mathrm{C2})$$

with an intrinsic scatter of 0.30 dex for the full sample and a scatter of 0.44 dex for the high-luminosity sources.

C.3. Physical Scale

Figure 9 shows the millimeter/X-ray luminosity ratio versus the physical beam scale of the 100 GHz ALMA observations. We concluded there is no correlation between the ratio and increasing the physical beam size, obtaining a p-value of 0.93. Therefore, we suggest that the excess in millimeter emission observed in our luminous sources is likely not primarily caused by the larger beam size compared to R23. However, future high-resolution observations will confirm this.

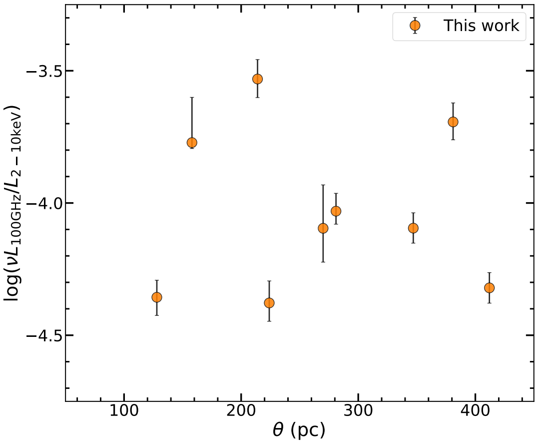

Figure 9. The millimeter/X-ray luminosity ratio $\log(\nu L_{100\mathrm{GHz}}/L_{2-10\mathrm{keV}})$ vs. the physical beam size θ of our ALMA observations in parsecs. We obtain a p-value of 0.93, which indicates that there is no correlation between the two parameters.

C.4. $L_{100GHz}/L_{2-10keV}$ Dependence on M_{BH} and SFR

Figure 10 displays the millimeter/X-ray luminosity ratio $\log(\nu L_{100\mathrm{GHz}}/L_{2-10\mathrm{keV}})$ as a function of M_{BH} and SFR. The lack of correlation we observe between the millimeter/X-ray luminosity ratio and M_{BH} and SFR and its implications are described in Section 5.2. The SFR values for seven out of nine sources, consisting of six upper limits and one detection, are adopted from K. Ichikawa et al. (2017, 2019) and were determined through IR SED decomposition. Finally, the SFR values for PG 0026+129 and PG 0052+251 were determined by Y. Díaz et al. (2026, in preparation) from the strength of the PAH feature.

C.5. X-Ray Outflows

To further investigate the potential connection between the observed millimeter emission and the presence of outflows, we analyzed the available high-quality X-ray spectra for the sources in our sample. Among the nine AGNs, five have archival X-ray observations with sufficiently high signal-to-noise ratios to enable a meaningful spectroscopic analysis aimed at identifying signatures of ionized absorption. In particular, we searched for evidence of absorbers or outflowing gas that could produce shocks and contribute to the observed millimeter continuum emission.

Q 0119–286 was observed by a short (∼9 ks) pointing by XMM-Newton. We extract the EPIC-pn spectrum using SASv20.0.0, from a circular region of 40″ that includes the source, and the background from a source-free region of the same size, after applying filters to remove bad time intervals with particle flaring and the processing command EPPROC. We fit the source with a model that includes neutral Galactic absorption ($N_{\mathrm{H}} = 1.5 \times 10^{20}\ \mathrm{cm}^{-2}$ HI4PI Collaboration et al. 2016), a blackbody to model a weak soft excess, a power law, and a Gaussian line for the Fe Kα emission line. We find a statistic of $\chi^2/\mathrm{dof} = 92/72$. The quality of this spectrum is not enough to use a photoionized grid; however, an absorption edge, typical of absorbers, is clearly present in a visual check of the residuals. Adding an edge model, we obtain an energy for the edge of $E = 620 \pm 35$ eV, marginally consistent with the oxygen K-edge at 540 eV. The statistic increases by $\Delta\chi^2/\Delta\mathrm{dof} = 14/2$ to $\chi^2/\mathrm{dof} = 78/70$, corresponding to a p-value of $p_{\mathrm{val}} = 0.0032$ ($\lesssim 3\sigma$). The blackbody temperature and the power-law photon index are $kT = 130 \pm 10$ eV and $\Gamma = 2.33 \pm 0.09$, respectively.

PG 0026+129 was observed for 13 ks by XMM-Newton and for 150 ks by NuSTAR. We model the spectra with an absorbed ($N_{\mathrm{H}} = 4.7 \times 10^{20}\ \mathrm{cm}^{-2}$; HI4PI Collaboration et al. 2016) power law plus blackbody and ionized reflection using XILLVER (J. García & T. R. Kallman 2010), prominent at $E > 10$ keV. Since a detailed fit is beyond the scope of this paper, we freeze the iron abundance and inclination of the disk in the model. The best-fit model has a statistic of $\chi^2/\mathrm{dof} = 1043/913$. Negative residuals are present in the soft X-ray band ($E = 0.5-2$ keV), strongly suggesting the presence of an absorber. We multiply the above model by our photoionized grid and the statistic improves to $\chi^2/\mathrm{dof} = 998/911$ ($\Delta\chi^2/\Delta\mathrm{dof} = 45/2$). This ionized gas is

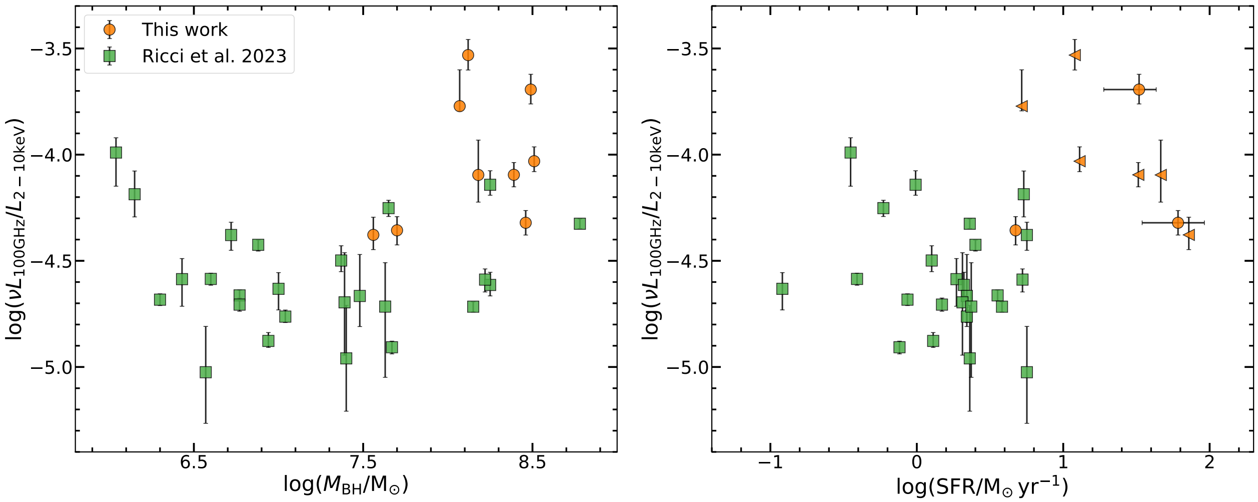

Figure 10. Left: the millimeter/X-ray luminosity ratio vs. the black hole mass M_{BH} of the sources from this work and R23. We find no correlation between the two, obtaining a p-value of 0.03. Right: the millimeter/X-ray luminosity ratio vs. the star formation rate (SFR). Eight out of nine sources in this work only have upper limits on SFR. No correlation is found, obtaining a p-value of 0.22.

characterized by column density $N_{\mathrm{H}} = (2 \pm 1) \times 10^{21}\,\mathrm{cm}^{-2}$ and a ionization parameter $\log \xi/(\mathrm{erg\,cm\,s}^{-1}) = 1.25^{+0.25}_{-0.50}$. We also retrieve a blackbody temperature $kT = 179 \pm 16$ eV, a photon index $\Gamma = 1.92^{+0.03}_{-0.05}$, and a cutoff energy $E_{\mathrm{cut}} = 94^{+82}_{-31}$ keV.

One source, PG 0052+251, was already studied by G. A. Matzeu et al. (2023) and a very low-ionization absorber ($\log \xi/(\mathrm{erg\,cm\,s}^{-1}) \sim -1.1$) with column density $N_{\mathrm{H}} \sim 6 \times 10^{21}\,\mathrm{cm}^{-2}$ was found.

Mrk 813 was observed 73 times with Swift-XRT and once by NuSTAR (OBSID 60160583002). All of the available XRT observations of Mrk 813 were combined into a single spectrum of ∼65 ks using the tool[36] described in P. A. Evans et al. (2009). In contrast, the FPMA and FPMB spectra (∼25 ks each) of the NuSTAR observations were extracted using NUSTARDAS, following the same procedure described by R. Serafinelli et al. (2024). The three spectra were fitted with a power law absorbed by Galactic absorption ($N_{\mathrm{H}} = 2.3 \times 10^{20}$; HI4PI Collaboration et al. 2016), plus a blackbody to phenomenologically model a moderate soft excess. We obtain a statistic of $\chi^2/\mathrm{dof} = 710/552$, where "dof" is the number of degrees of freedom of the fit. Clear residuals are present at ∼1 keV, which might indicate the presence of an absorber through the presence of an Fe UTA absorption complex (e.g., J. P. Halpern 1984; E. Behar et al. 2003; A. J. Blustin et al. 2005; S. Laha et al. 2014; R. Serafinelli et al. 2025). We create a photoionization grid using XSTAR (T. Kallman & M. Bautista 2001). Following, e.g., F. Tombesi et al. (2011) and R. Serafinelli et al. (2019), we assume an SED with $\Gamma = 2$, $E_{\mathrm{cut}} = 100$ keV, solar abundances (M. Asplund et al. 2009), a fully covering medium (covering factor $C_f = 1$), and a turbulent velocity of $v_{\mathrm{turb}} = 100\,\mathrm{km\,s}^{-1}$ (e.g., S. Laha et al. 2014). We apply the photoionization grid, and we find $N_{\mathrm{H,ion}} = 3.4^{+0.8}_{-0.6} \times 10^{21}\,\mathrm{cm}^{-2}$ and a ionization parameter upper limit of $\log \xi/(\mathrm{erg\,cm\,s}^{-1}) < 0.8$. The continuum photon index is $\Gamma = 1.87 \pm 0.03$, while the blackbody temperature is $kT = 84^{+22}_{-6}$ eV. The statistic improves by $\Delta\chi^2/\Delta\mathrm{dof} = 101/2$ to a final $\chi^2/\mathrm{dof} = 609/500$, indicating that the absorber is extremely significant. We note that although our best fit is consistent with neutral absorption since we found an upper limit to the ionization parameter, the adoption of a neutral absorption model is disfavored by a much smaller improvement of the fit statistic ($\Delta\chi^2/\Delta\mathrm{dof} = 13/1$).

As discussed in Section 3.2, we found evidence for the presence of an absorber in 2MASX J02223523+2508143. We analyzed the archival Swift/XRT observations of this source, combining all available exposures to obtain a spectrum with ∼3500 counts. The spectral fitting was performed in XSPEC following the same procedure adopted for the other sources. The spectrum clearly reveals the presence of ionized absorption. We modeled this component with our standard XSTAR table. The best-fit absorber has a column density of $N_{\mathrm{H}} = (8.8 \pm 2.2) \times 10^{21}\,\mathrm{cm}^{-2}$, and ionization parameter $\log \xi/(\mathrm{erg\,cm\,s}^{-1}) = 0.9 \pm 0.2$. In addition to the continuum, two emission features were required by the fit: a soft line at ∼0.7 keV, and the neutral Fe Kα line at 6.4 keV. The primary X-ray continuum was well described by a power law with photon index $\Gamma = 1.94 \pm 0.15$. The overall fit is statistically acceptable ($\chi^2/\mathrm{dof} = 103/124$).

Finally, the remaining source with X-ray observations of sufficient quality for spectral analysis is LEDA 12773, for which 30 Swift-XRT exposures were combined into a total effective exposure time of 65 ks, following the procedure described by P. A. Evans et al. (2009). For this source, we do not detect any evidence of ionized X-ray absorption. The spectrum is well fitted by a model consisting of a power law plus blackbody component, absorbed by Galactic neutral hydrogen ($N_{\mathrm{H}} = 10^{20}\,\mathrm{cm}^{-2}$; HI4PI Collaboration et al. 2016), yielding a fit statistic of $\chi^2/\mathrm{dof} = 547/665$.

C.6. Spectral Index Dependence on AGN Parameters

Figure 11 displays the millimeter spectral index α_{mm} as a function of the Eddington ratio λ_{Edd}. We obtain a p-value of 0.17 and, therefore, determine no correlation. Figure 11 also displays the bolometric luminosity L_{bol} as a function of the Eddington ratio λ_{Edd}. We obtain a p-value of 0.37, which indicates no correlation between the two parameters. Finally, we present α_{mm} as a function of SFR in Figure 11, where no correlation is observed either, obtaining a p-value of 0.85.

---

[36] https://www.swift.ac.uk/user_objects/

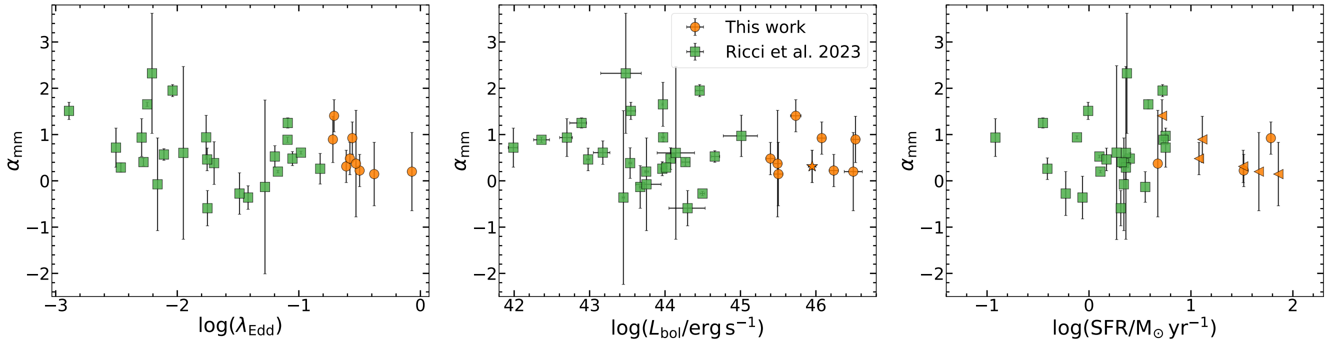

Figure 11. Left: spectral index ($\alpha_{\rm mm}$) of the 100 GHz observations for this work, as obtained from fitting $S_{\rm mm} \propto \nu^{-\alpha_{\rm mm}}$ to the 100 GHz fluxes in mJy in the four separate SPWs, and R23 vs. the Eddington ratio $\lambda_{\rm Edd}$. We do not observe a correlation, obtaining a p-value of 0.17. Middle: $\alpha_{\rm mm}$ vs. the bolometric luminosity $L_{\rm bol}$. Here, no correlation is observed either since we obtain a p-value of 0.37. Right: $\alpha_{\rm mm}$ vs. SFR. We obtain a p-value of 0.85, observing no correlation.

C.7. Radio-to-submillimeter SEDs

To determine whether the observed millimeter emission in our high-luminosity AGNs can be fully attributed to the X-ray corona, we performed an SED fitting procedure following the work by S. del Palacio et al. (2025). We present below the available ancillary data in addition to our ALMA Band 3 observations, along with the SED fitting results for the sources in our sample. The best-constrained SEDs are shown in Figure 4 in Section 5.3.3.

For Q 0019–286, the SED is very poorly constrained, with only upper limits from the Rapid ASKAP Continuum Survey (RACS) and the Very Large Array Sky Survey (VLASS). While the 100 GHz ALMA flux could be dominated by free–free emission, a corona with $r_{\rm c} \sim 110$ and $\log \delta \sim -2.30$ could potentially be consistent with the SED fit.

PG 0026+129 has one of the best-constrained SEDs, thanks to VLA data in Bands C (4–8 GHz) and Q (40–50 GHz) and VLBA data at 1.5, 5.0, 8.4, and 23.6 GHz. The fit (see Figure 4) indicates that the 100 GHz flux is dominated by a corona with $r_{\rm c} = 217 \pm 13$ and $\log \delta = -1.06 \pm 0.11$. More details can be found in Section 5.3.3.

PG 0052+251 has a less constrained SED, presented in Figure 4 as well, with VLA data in Bands C, X, and Q, VLBA data, and ALMA Band 5 data (187–202 GHz; Proposal ID 2023.1.01062.S; PI: F. Bauer). The 100 GHz flux could be constrained by a corona with $r_{\rm c} = 131 \pm 66$ and $\log \delta = -1.68^{+0.31}_{-1.17}$, although this fit is more ambiguous compared to PG 0026+129. More details on this fit can be found in Section 5.3.3 as well.

For Mrk 813, the SED is poorly constrained, having only additional upper limits from RACS and VLASS, along with VLA C-band data. The 100 GHz flux should arise exclusively from the corona, although the peak of the SED is highly uncertain. The derived parameters span a wide range: $r_{\rm c} \sim 380 \pm 200$ and $\log \delta \sim -2.3 \pm 0.3$.

For RHS 61, we combined the 100 GHz data with upper limits from the low-resolution LoTSS, RACS, and VLASS surveys, as well as VLA C-band data. The corona is poorly constrained, and a significant fraction of the 100 GHz flux could originate from free–free emission. The SED fit is consistent with a corona of size $r_{\rm c} \sim 200$ and $\log \delta \sim -2.0$.

LEDA 126226 has a loosely constrained SED, with only low-resolution survey data available. The 100 GHz flux could be dominated by a corona with $r_{\rm c} \sim 550$ and $\log \delta \sim -1.5$, but these values are highly uncertain, and free–free emission may contribute significantly.

For 2MASX J02223523+2508143, the SED is also very loosely constrained, with only RACS and VLASS data. The 100 GHz flux could primarily originate from the corona if $r_{\rm c} \sim 400$ and $\log \delta \sim -2.3$, but these parameters are poorly determined.

Similarly, for 2MASX J17311341+1442561, the SED is very loosely constrained, with only RACS and VLASS data. The 100 GHz flux may come mostly from a corona with $r_{\rm c} \sim 300$ and $\log \delta \sim -2.3$, although the constraints are weak.

Finally, for LEDA 12773, the SED is very poorly constrained, with only low-resolution RACS and VLASS data. The 100 GHz flux could be dominated by a corona with $r_{\rm c} \sim 300$ and $\log \delta \sim -2.6$.

ORCID iDs

Sophie M. Venselaar https://orcid.org/0009-0001-8342-7522
Claudio Ricci https://orcid.org/0000-0001-5231-2645
Santiago Del Palacio https://orcid.org/0000-0002-5761-2417
Kriti K. Gupta https://orcid.org/0009-0007-9018-1077
Chin-Shin Chang https://orcid.org/0000-0001-9910-3234
Roberto Serafinelli https://orcid.org/0000-0003-1200-5071
Macon A. Magno https://orcid.org/0000-0002-1292-1451
Richard Mushotzky https://orcid.org/0000-0002-7962-5446
Elena Shablovinskaya https://orcid.org/0000-0003-2914-2507
Taiki Kawamuro https://orcid.org/0000-0002-6808-2052
Ezequiel Treister https://orcid.org/0000-0001-7568-6412
Jacob S. Elford https://orcid.org/0000-0002-6139-2226
Susanne Aalto https://orcid.org/0000-0002-5828-7660
George C. Privon https://orcid.org/0000-0003-3474-1125
Michael J. Koss https://orcid.org/0000-0002-7998-9581

References

Ackermann, M., Ajello, M., Allafort, A., et al. 2012, ApJ, 747, 104
Arnaud, K. A. 1996, ASPC, 101, 17
Asplund, M., Grevesse, N., Sauval, A. J., & Scott, P. 2009, ARA&A, 47, 481
Avni, Y., & Tananbaum, H. 1982, ApJ, 262, L17
Avni, Y., & Tananbaum, H. 1986, ApJ, 305, 83
Baldi, R. D., Behar, E., Laor, A., & Horesh, A. 2015, MNRAS, 454, 4277
Baldi, R. D., Laor, A., Behar, E., et al. 2022, MNRAS, 510, 1043
Baumgartner, W. H., Tueller, J., Markwardt, C. B., et al. 2013, ApJS, 207, 19
Behar, E., Baldi, R. D., Laor, A., et al. 2015, MNRAS, 451, 517
Behar, E., Kaspi, S., Paubert, G., et al. 2020, MNRAS, 491, 3523
Behar, E., Rasmussen, A. P., Blustin, A. J., et al. 2003, ApJ, 598, 232

Behar, E., Vogel, S., Baldi, R. D., Smith, K. L., & Mushotzky, R. F. 2018, MNRAS, 478, 399
Blustin, A. J., Page, M. J., Fuerst, S. V., Branduardi-Raymont, G., & Ashton, C. E. 2005, A&A, 431, 111
Breeveld, A. A., Curran, P. A., Hoversten, E. A., et al. 2010, MNRAS, 406, 1687
Brinchmann, J., Charlot, S., White, S. D. M., et al. 2004, MNRAS, 351, 1151
Burrows, D. N., Hill, J. E., Nousek, J. A., et al. 2005, SSRv, 120, 165
CASA Team, Bean, B., Bhatnagar, S., et al. 2022, PASP, 134, 114501
Cash, W. 1979, ApJ, 228, 939
Cerqueira-Campos, F. C., Rodríguez-Ardila, A., Riffel, R., et al. 2021, MNRAS, 500, 2666
Chen, S., Laor, A., Behar, E., et al. 2025, ApJ, 979, 241
Condon, J. J., Cotton, W. D., Greisen, E. W., et al. 1998, AJ, 115, 1693
Curran, P. A. 2014, arXiv:1411.3816
del Palacio, S., Yang, C., Aalto, S., et al. 2025, A&A, 701, A41
den Brok, M., Carollo, C. M., Erroz-Ferrer, S., et al. 2020, MNRAS, 491, 4089
Di Matteo, T. 1998, MNRAS, 299, L15
Droguett-Callejas, M., Treister, E., Barcos-Muñoz, L., et al. 2026, ApJL, 999, L11
Duras, F., Bongiorno, A., Ricci, F., et al. 2020, A&A, 636, A73
Evans, P. A., Beardmore, A. P., Page, K. L., et al. 2009, MNRAS, 397, 1177
Fabian, A. C., Lohfink, A., Belmont, R., Malzac, J., & Coppi, P. 2017, MNRAS, 467, 2566
Field, G. B., & Rogers, R. D. 1993, ApJ, 403, 94
Fiore, F., Feruglio, C., Shankar, F., et al. 2017, A&A, 601, A143
García, J., & Kallman, T. R. 2010, ApJ, 718, 695
GRAVITY Collaboration, Amorim, A., Bauböck, M., et al. 2021, A&A, 648, A117
Gupta, K. K., Ricci, C., Temple, M. J., et al. 2024, A&A, 691, A203
Gupta, K. K., Ricci, C., Tortosa, A., et al. 2025, ApJ, 990, 86
Haardt, F., & Maraschi, L. 1991, ApJL, 380, L51
Halpern, J. P. 1984, ApJ, 281, 90
Hankla, A. M., Philippov, A., Mbarek, R., et al. 2026, ApJ, 997, 224
Harris, C. R., Millman, K. J., van der Walt, S. J., et al. 2020, Natur, 585, 357
HI4PI Collaboration, Ben Bekhti, N., Flöer, L., et al. 2016, A&A, 594, A116
Hickox, R. C., & Alexander, D. M. 2018, ARA&A, 56, 625
Hildebrand, R. H. 1983, QJRAS, 24, 267
Hwang, H.-C., Zakamska, N. L., Alexandroff, R. M., et al. 2018, MNRAS, 477, 830
Ichikawa, K., Ricci, C., Ueda, Y., et al. 2017, ApJ, 835, 74
Ichikawa, K., Ricci, C., Ueda, Y., et al. 2019, ApJ, 870, 31
Inoue, Y., & Doi, A. 2014, PASJ, 66, L8
Inoue, Y., & Doi, A. 2018, ApJ, 869, 114
Inoue, Y., Takasao, S., & Khangulyan, D. 2024, PASJ, 76, 996
Isobe, T., Feigelson, E. D., & Nelson, P. I. 1986, ApJ, 306, 490
Jiang, Y.-F., Ciotti, L., Ostriker, J. P., & Spitkovsky, A. 2010, ApJ, 711, 125
Kallman, T., & Bautista, M. 2001, ApJS, 133, 221
Katz, J. I. 1976, ApJ, 206, 910
Kawamuro, T., Ricci, C., Imanishi, M., et al. 2022, ApJ, 938, 87
Kawamuro, T., Ricci, C., Mushotzky, R. F., et al. 2023, ApJS, 269, 24
Koss, M., Trakhtenbrot, B., Ricci, C., et al. 2017, ApJ, 850, 74
Koss, M. J., Trakhtenbrot, B., Ricci, C., et al. 2022, ApJS, 261, 1
Koss, M. J., Treister, E., Kakkad, D., et al. 2023, ApJL, 942, L24
Laha, S., Guainazzi, M., Dewangan, G. C., Chakravorty, S., & Kembhavi, A. K. 2014, MNRAS, 441, 2613
Laor, A., & Behar, E. 2008, MNRAS, 390, 847
Liu, J.-R., Wang, J.-M., Fermi-LAT Collaboration, et al. 2025, NatAs, 9, 1086
Lusso, E., Comastri, A., Vignali, C., et al. 2010, A&A, 512, A34
Malizia, A., Molina, M., Bassani, L., et al. 2014, ApJ, 782, L25
Markoff, S., Nowak, M. A., & Wilms, J. 2005, ApJ, 635, 1203
Martocchia, S., Piconcelli, E., Zappacosta, L., et al. 2017, A&A, 608, A51
Matzeu, G. A., Brusa, M., Lanzuisi, G., et al. 2023, A&A, 670, A182
McMullin, J. P., Waters, B., Schiebel, D., Young, W., & Golap, K. 2007, ASPC, 376, 127
Michiyama, T., Inoue, Y., Doi, A., et al. 2024, ApJ, 965, 68
Mullaney, J. R., Alexander, D. M., Goulding, A. D., & Hickox, R. C. 2011, MNRAS, 414, 1082
Nhat Ly, M., Inoue, Y., Sentoku, Y., & Sano, T. 2026, ApJ, 1004, 27
Nims, J., Quataert, E., & Faucher-Giguère, C.-A. 2015, MNRAS, 447, 3612
Noeske, K. G., Faber, S. M., Weiner, B. J., et al. 2007, ApJL, 660, L47
Padovani, P. 2017, NatAs, 1, 0194
Padovani, P., Miller, N., Kellermann, K. I., et al. 2011, ApJ, 740, 20
Panessa, F., Baldi, R. D., Laor, A., et al. 2019, NatAs, 3, 387
Paul, J. D., & Plotkin, R. M. 2026, ApJ, 998, 296
Pei, Y. C. 1992, ApJ, 395, 130
Peng, C. Y., Ho, L. C., Impey, C. D., & Rix, H.-W. 2002, AJ, 124, 266
Peng, C. Y., Ho, L. C., Impey, C. D., & Rix, H.-W. 2010, AJ, 139, 2097
Petrucci, P. O., Piétu, V., Behar, E., et al. 2023, A&A, 678, L4
Piconcelli, E., Bianchi, S., Vignali, C., Jiménez-Bailón, E., & Fiore, F. 2011, A&A, 534, A126
Poole, T. S., Breeveld, A. A., Page, M. J., et al. 2008, MNRAS, 383, 627
Privon, G. C., Ricci, C., Aalto, S., et al. 2020, ApJ, 893, 149
Ramos Almeida, C., & Ricci, C. 2017, NatAs, 1, 679
Reeves, J., Done, C., Pounds, K., et al. 2008, MNRAS, 385, L108
Ricci, C. 2026, Encyclopedia of Astrophysics, Vol. 4 (Elsevier), 210
Ricci, C., Chang, C.-S., Kawamuro, T., et al. 2023, ApJ, 952, L28
Ricci, C., Ho, L. C., Fabian, A. C., et al. 2018, MNRAS, 480, 1819
Ricci, C., Trakhtenbrot, B., Koss, M. J., et al. 2017, ApJS, 233, 17
Ricci, C., Ueda, Y., Koss, M. J., et al. 2015, ApJ, 815, L13
Rodríguez-Ardila, A., May, D., Panda, S., Fonseca-Faria, M. A., & Fraga, L. 2024, MNRAS, 527, 10649
Rybak, M., Sluse, D., Gupta, K. K., et al. 2025, A&A, 701, A215
Scholz, F. W., & Stephens, M. A. 1987, JASA, 82, 918
Serafinelli, R., De Rosa, A., Tortosa, A., et al. 2024, A&A, 690, A145
Serafinelli, R., Nicastro, F., Luminari, A., et al. 2025, ApJ, 995, 6
Serafinelli, R., Tombesi, F., Vagnetti, F., et al. 2019, A&A, 627, A121
Shablovinskaia, E., Ricci, C., Paladino, R., et al. 2025, A&A, 703, A82
Shablovinskaya, E., Ricci, C., Chang, C.-S., et al. 2024, A&A, 690, A232
Tananbaum, H., Avni, Y., Branduardi, G., et al. 1979, ApJ, 234, L9
Teng, S. H., Mushotzky, R. F., Sambruna, R. M., Davis, D. S., & Reynolds, C. S. 2011, ApJ, 742, 66
Tombesi, F., Cappi, M., Reeves, J. N., et al. 2011, ApJ, 742, 44
Tortosa, A., Bianchi, S., Marinucci, A., Matt, G., & Petrucci, P. O. 2018, A&A, 614, A37
Vasudevan, R. V., & Fabian, A. C. 2007, MNRAS, 381, 1235
Vasudevan, R. V., & Fabian, A. C. 2009, MNRAS, 392, 1124
Virtanen, P., Gommers, R., Burovski, E., et al. 2020, scipy/scipy: SciPy 1.6.0, v1.6.0, Zenodo, doi:10.5281/zenodo.4406806
Virtanen, P., Gommers, R., Oliphant, T. E., et al. 2020, NatMe, 17, 261
Wilkes, B. J., Tananbaum, H., Worrall, D. M., et al. 1994, ApJS, 92, 53
Wilms, J., Allen, A., & McCray, R. 2000, ApJ, 542, 914
Yamada, T., Sakai, N., Inoue, Y., & Michiyama, T. 2024, ApJ, 968, 116
Zappacosta, L., Piconcelli, E., Giustini, M., et al. 2020, A&A, 635, L5